Journal of The Electrochemical Society, 2021 **168** 064521

Degradation Mechanism of an IrO2 Anode Co-Catalyst for Cell Voltage Reversal Mitigation under Transient Operation Conditions of a PEM Fuel Cell

Mohammad Fathi Tovini,[1,*,z] Ana Marija Damjanovic,[1,*] Hany A. El-Sayed,[1] Jozsef Speder,[2] Christian Eickes,[2] Jens-Peter Suchsland,[2] Alessandro Ghielmi,[2] and Hubert A. Gasteiger[1,]**

[1]*Chair of Technical Electrochemistry, Department of Chemistry and Catalysis Research Center, Technical University of Munich, 85748 Garching, Germany*
[2]*Greenerity GmbH, 63457 Hanau-Wolfgang, Germany*

IrO_2 is the most stable oxygen evolution reaction (OER) catalyst in acidic media and it has been widely used as co-catalyst to mitigate cell reversal damages in the anode of PEM fuel cells (PEMFCs). In this study, a mechanistic understanding of the degradation of an IrO_2 anode co-catalyst under transient operation of a PEMFC is provided. Thermogravimetric analysis (TGA) in reductive atmosphere (3.3 vol.% H_2/Ar) shows that IrO_2 is not stable in H_2 containing atmosphere at operational temperatures of PEMFCs. By conducting a series of physical-chemical and electrochemical analyses, it is proven that H_2 under the operating conditions in a PEMFC anode can chemically reduce a few outer monolayers of the surface of IrO_2 nanoparticles to metallic Ir. The metallic Ir formed on the IrO_2 surface can then dissolve during fuel cell start-up/shut-down (SUSD) cycles. At least part of the dissolved Ir species formed in the anode electrode are shown to diffuse through the membrane to the cathode electrode, where they lead to a deterioration of the oxygen reduction reaction (ORR) activity of the Pt cathode catalyst. The consequences of Ir dissolution on the cell reversal tolerance of the anode are also discussed.
 [DOI: 10.1149/1945-7111/ac0d39]

Manuscript submitted March 22, 2021; revised manuscript received June 10, 2021. Published June 28, 2021.

One of the challenges that hinders the widespread commercialization of fuel cell electric vehicles is meeting long-term durability targets.[1] Among several conditions that can cause a substantial degradation of membrane electrode assemblies (MEAs), cell (voltage) reversal has recently received a great attention.[2–4] Cell reversal can occur during the transient operation of proton exchange membrane fuel cells (PEMFCs) on account of a temporary undersupply of H_2 to one or several cells in a fuel cell stack.[2–5] During cell reversal events, the anode potential rises to $\gg$1 V vs the reversible hydrogen electrode (RHE) potential, causing a transient dissolution of platinum and a continuous oxidation of the carbon support:

$$C + 2H_2O \rightarrow CO_2 + 4H^+ + 4e^- \quad [1]$$

The carbon oxidation reaction (COR) according to Eq. 1 is thermodynamically favorable at potentials >0.2 V_{RHE}, but due to its slow kinetics, considerable rates are only observed at potentials >0.9 V_{RHE};[6–8] such high anode potentials occur during cell reversal and lead to a collapse of the anode catalyst layer and to cell failure. There are three main strategies to mitigate the damages caused by cell reversal: i) replacing the carbon support by corrosion resistant support materials such as metal oxides;[9,10] ii) application of system-mitigation strategies;[11,12] and, iii) addition of a co-catalyst to the anode electrode which catalyzes the oxygen evolution reaction (OER), so that the non-destructive OER, rather than the destructive COR, will take place.[2,4,5,13,14] The application of corrosion resistant non-carbon support materials has been limited due to their generally lower electrical conductivity, their often insufficient stability particularly at transient fuel cell operating conditions, the risk of cationic contamination and/or degradation of the ionomer in membrane and electrodes, and cost considerations[15–17]; therefore, graphitized carbons are the currently used support materials for Pt-based anode catalysts for the hydrogen oxidation reaction (HOR) in PEMFC stacks.[5] On the other hand, the implementation of system-mitigation strategies adds complexity and cost to the PEMFC system: as cell reversal damages can be substantial even if the cell reversal only occurs over time scales of tens of milliseconds, the control system has to be able to detect cell reversals on a millisecond time scale and to respond very quickly to prevent MEA damage. Therefore, addition of an OER co-catalyst to the anode electrode would seem to be the most simple strategy to mitigate cell reversal damages, and a commonly used anode co-catalyst to facilitate the OER over the COR during cell reversal events is iridium oxide (IrO_2).[2,4,14,18–20]

Numerous studies have investigated the effect of IrO_2 co-catalysts on mitigating cell reversal degradation in PEMFC anodes. It is well known that the OER activity of an IrO_2 catalyst reliably correlates with the effectiveness of the catalyst for mitigating cell reversal degradation in a PEMFC.[20] The low onset potential of the OER on IrO_2 prevents the anode potential from reaching high values during cell reversal, and thus significantly reduces the extent of the COR at the anode side. Therefore, the focus of the research in this field is to attain highly OER-active IrO_2 catalysts by different synthesis approaches and to modify the anode catalyst layer design such as to achieve a uniform dispersion of IrO_2 in the anode catalyst layer.[18–21] Typically, the mitigation performance of an anode OER co-catalyst is evaluated by simulated cell reversal tests (CRTs) in single-cell PEMFCs, in which a constant current (typically 0.2 Acm^{-2}) is applied with air flowing through the cathode compartment and N_2 (rather than H_2) flowing through the anode compartment.[5,22,23] Due to the lack of H_2 on the anode electrode during the CRT, the cell potential vs time rapidly drops to large negative values in the beginning of the CRT and then reaches a nearly constant potential plateau whose value gradually decreases over time, until it results in a drastic potential drop that is considered to mark the complete degradation of the anode catalyst layer. The time spent until this final potential drop is usually taken as a figure-of-merit to compare the performance of different anode co-catalysts during cell reversal. The negative cell potential during the CRT corresponds to the difference between the positive cathode potential that is established at the cell current by the ORR on the cathode catalyst and the more positive anode potential at which the cell current can be supplied by the OER and the COR reaction at the anode. Thus, the higher the OER activity of the anode co-catalyst, the less positive will be the anode potential during the CRT,

*Electrochemical Society Student Member.
**Electrochemical Society Fellow.
[z]E-mail: m.fathi@tum.de

resulting in a lower rate of the COR at the anode and, consequently, in a higher cell reversal tolerance.

In addition to the high OER activity of the anode co-catalyst, another requirement a co-catalyst needs to fulfil is that it should be stable under the normal operating conditions of a PEMFC anode. While we are not aware of any comprehensive study on the stability of IrO_2 in the H_2 atmosphere in a PEMFC anode, experiments in a PEM water electrolyzer configuration show that it will undergo surface reduction under these conditions.[24] This could ultimately affect the stability of an IrO_2 anode co-catalyst, particularly during the repetitive transitions between normal operating conditions, where the anode potential is at $\sim$0 V_{RHE}, and the high anode potentials ($\geqslant$1 V_{RHE}) that occur during cell reversal and system start-up/shut-down (SUSD) transients. An SUSD transient takes place when a H_2/air_{anode}-front passes through the anode flow field due to the replacement of the H_2 gas by air during shut-down and vice versa during start-up.[25] The underlying degradation mechanism during SUSD and the effect of various conditions were subject to many studies. It has been shown that SUSD does not only invoke oxidative currents in the cathode electrode, which leads to carbon corrosion and loss of Pt electrochemical surface area (ECSA) at the cathode,[26,27] but that it also leads to a significant Pt ECSA loss at the anode induced by the anode potential cycling between $\sim$0 and $\sim$1 V_{RHE} upon the passage of H_2/air_{anode} front.[28] These anode voltage cycles enhance the dissolution of an IrO_2 catalyst that has been exposed to H_2 at elevated temperatures (80 °C), as indicated in a recent publication from our group. There, we have shown that H_2 permeating through the membrane from the hydrogen cathode to the oxygen anode of a PEM water electrolyzer (PEMWE) during open circuit voltage (OCV) conditions leads to a surface reduction of an IrO_2 OER catalyst to metallic Ir, which in turn gets oxidized to an amorphous IrO_x during the subsequent normal operation period of the PEMWE at the high OER potentials.[29] The repetitive cycling between the reducing conditions during OCV periods, where the surface of the IrO_2 catalyst is reduced to metallic Ir, and oxidizing conditions during operation, where the IrO_2 surface is re-oxidized to an amorphous IrO_x, were shown to cause an enhanced dissolution of iridium, concomitant with iridium redeposition in the membrane.

In this study, we examine the cell reversal tolerance in the presence of an IrO_2 anode co-catalyst as well as its degradation and concomitant poisoning of the cathode catalyst activity upon SUSD cycles. Thermogravimetric analysis (TGA) in reductive atmosphere (3.3 vol.% H_2/Ar) is used to simulate the reductive environment of PEMFC anode during normal operation, and shows that the near-surface region of IrO_2 can be completely reduced to metallic Ir under the operating conditions of a PEMFC anode. The formation of metallic iridium surfaces after TGA experiments to different temperature is proven by X-ray photoelectron spectroscopy (XPS), and we show that the same surface reduction occurs in an MEA upon extended exposure of IrO_2 to H_2 in a PEMFC anode. Finally, it is shown that anode potential transients, such as those caused by SUSD events, lead to the dissolution of iridium from the IrO_2 based anode co-catalyst. Subsequently, the dissolved iridium is shown to diffuse through the membrane and to poison the oxygen reduction reaction (ORR) activity of the cathode catalyst, which deteriorates the cell performance. In summary, we will investigate the fundamental aspects of the stability of IrO_2 in the presence of H_2 using different physical-chemical and electrochemical diagnostics (see left panel of Fig. 1). Following this, the effect of partial reduction of IrO_2 in a PEMFC anode condition when used as an anode co-catalyst is investigated on the durability of PEMFCs upon intermittent operation, namely cell reversal and SUSD (see right panel of Fig. 1).

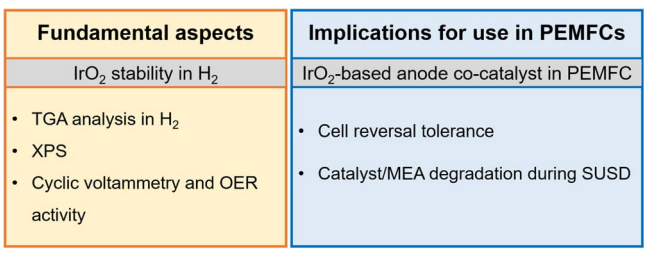

Figure 1. A schematic overview of the two main experimentally designed sections in this work and the experiments which are performed in each section.

Experimental

IrO_2/TiO_2 catalyst specification.—A commercial benchmark IrO_2 supported on TiO_2 OER catalyst (IrO_2/TiO_2 with 75 wt.% iridium, Elyst Ir75 0480 from Umicore, Germany) is used throughout this study. According to the patent, the IrO_2 deposited onto the high surface area TiO_2 is heat-treated ($T_{heat\text{-}treatment} \approx$ 400 °C in air atmosphere),[30] and it has previously been shown by our group that it is an active and stable OER catalyst for PEMWE applications.[31,32] A stoichiometric IrO_2 (iridium(IV) oxide) consists of 85.7 wt.% Ir and 14.3 wt.% O. Considering that the here used IrO_2/TiO_2 catalyst consists of 75 wt.% Ir, its nominal composition can be calculated as: 87.5 wt.% IrO_2 (75 wt.% Ir, 12.5 wt.% O_{IrO2}) and 12.5 wt.% TiO_2 (7.5 wt.% Ti, 5 wt.% O_{TiO2}). During TGA experiments under H_2, the IrO_2 phase of this catalyst can be reduced according to the following reaction:

$$IrO_2(s) + 2H_2(g) \rightarrow Ir(s) + 2H_2O(g) \quad [2]$$

Considering that TiO_2 cannot be reduced at temperatures where IrO_2 will be fully reduced (i.e., at 350 °C, as will be shown later), the total mass loss of the IrO_2/TiO_2 catalyst upon the complete reduction of IrO_2 to Ir would be accompanied by the total loss of O_{IrO2}, which would amount to a mass loss of the IrO_2/TiO_2 catalyst of 12.5 wt.%.

Next we will estimate the mass loss upon the reduction of a monolayer of IrO_2, assuming a core–shell morphology, with the surface of the TiO_2 support covered completely by IrO_2 particles. This assumption should be quite reasonable in view of the fact that the IrO_2 that is deposited on the TiO_2 support has a volume fraction of $\sim$72% in the final IrO_2/TiO_2 catalyst (based on $\rho_{IrO2} = 11.7\ g\ cm^{-3}$ and $\rho_{TiO2} = 4.23\ g\ cm^{-3}$). Furthermore, since no Ti signal is detected in the XPS Ti2p spectrum of as-received IrO_2/TiO_2 catalyst (see Fig. A·1), it can be deduced that the TiO_2 support particles are completely covered by the IrO_2 particles. Based on the patent,[30] the pristine TiO_2 particles for the preparation of this IrO_2/TiO_2 catalyst have a specific surface area of 50 $m^2 g^{-1}_{TiO2}$. This corresponds to an average calculated TiO_2 particle size of $d \approx 28$ nm. Considering that the final IrO_2/TiO_2 catalyst contains 87.5 wt.% IrO_2 along with the assumption that TiO_2 particles are covered by a uniform and compact film of crystalline IrO_2, an equivalent IrO_2 film thickness of $\sim$7.5 nm covering TiO_2 support particles can be calculated for the IrO_2/TiO_2 catalyst. The specific surface area of this catalyst determined by the Brunauer–Emmett–Teller (BET) method is 27.2 $m^2 g^{-1}_{IrO2/TiO2}$. By assuming a complete coverage of the TiO_2 support by IrO_2 particles (the schematic in Fig. A·1, inset, shows such a structural assumption), all of the physisorbed N_2 determined by the BET measurement would be adsorbed on the outermost IrO_2 surface, so that the BET surface area of 27.2 $m^2 g^{-1}_{IrO2/TiO2}$ would represent the area of exposed IrO_2 in 1 g of catalyst ($S_{BET(IrO2)}$). For a zero order estimate of the molar amount of IrO_2 in the outermost monolayer of the IrO_2 phase, we consider the hypothetical case that all of the IrO_2 in the IrO_2/TiO_2 catalyst would be in the rutile phase, so that the IrO_2 surface area can be calculated from the theoretical ionic radii of O^{2-} and Ir^{4+} in a rutile structure. While a significant fraction of the IrO_2 phase is actually amorphous, it still has an oxidation state of +4 (see discussion of Fig. 2a), so that the thus estimated surface area should still be reasonable. With this approximation and the above determined BET surface area, one can then estimate the molar amount of IrO_2 in the outermost monolayer of the IrO_2 phase in 1 g of the

IrO_2/TiO_2 catalyst ($n_{IrO2(ML)}$):

$$n_{IrO2(ML)} = \frac{S_{BET(IrO2)}}{S_{IrO2}\cdot N_A} = \frac{27.2 m^2_{IrO2}}{(1.18\cdot10^{-19} m^2_{IrO2})\cdot(6.022\cdot10^{23})} = 3.83\cdot10^{-4} mol_{IrO2}\, g^{-1}_{IrO2/TiO2} \quad [3]$$

where S_{IrO2} is the cross-sectional area of an IrO_2 unit, estimated from the area of two O^{2-} ions and one Ir^{4+} ion based on their ionic radii (O^{2-} = 126 pm, Ir^{4+} = 76.5 pm),[33] yielding $S_{IrO2} = 1.18 \cdot 10^{-19}$ m^2_{IrO2}, and where N_A is Avogadro's number (6.022×10^{23}). Considering that the catalyst contains 87.5 wt.% IrO_2 with a molecular mass of 224 g mol^{-1}, the total moles of IrO_2 in the IrO_2/TiO_2 catalyst is $n_{IrO2(total)} = 3.90 \cdot 10^{-3}$ $mol_{IrO_2}\, g^{-1}_{IrO_2/TiO_2}$. Therefore, the molar fraction of IrO_2 that is on the outermost surface of the assumed iridium shell amounts to:

$$x_{IrO_2(ML)} = \frac{n_{IrO_2(ML)}}{n_{IrO_2(total)}} = \frac{3.83\cdot10^{-4} mol}{3.90\cdot10^{-3} mol} = 0.098 \quad [4]$$

According to this estimate, one monolayer of IrO_2 (ML_{IrO_2}) on the IrO_2/TiO_2 catalyst corresponds to ~10% of the total moles of IrO_2 in the catalyst. Therefore, the reduction of 1 ML_{IrO2} and, consequently, the formation of 1 monolayer metallic Ir (ML_{Ir}) on the surface of the IrO_2/TiO_2 catalyst via reaction [2], corresponds to the reduction of ~10% of the total moles of IrO_2 in the IrO_2/TiO_2 catalyst. Referenced to the overall IrO_2/TiO_2 mass, the reduction of 1 ML_{IrO2} thus corresponds to an overall mass loss of ~0.1 · 12.5 wt.% ≈ 1.25 wt.%, a value which can be used to judge the extent of IrO_2 reduction during the later shown TGA experiments with the IrO_2/TiO_2 catalyst.

Rotating disk electrode (RDE) measurements.—Electrochemical measurements were carried out in a three-electrode cell using a static H_2 reference electrode (RE) consisted of a Pt wire sealed into one end of a glass tube which was drawn to a capillary and filled with electrolyte and a bubble of evolved H_2 (all voltages of RDE experiments throughout this work are quoted vs the potential of this reversible hydrogen electrode (V_{RHE})),[34] a high surface area Au wire as a counter electrode (CE), and a 5 mm diameter polycrystalline Au disk working electrode (WE) assembled in an interchangeable rotating ring-disk electrode (RRDE) shaft made of polyether ketone (Pine Research Instrumentation, USA). The reference electrode potential was calibrated in a H_2 saturated electrolyte prior to each experiment using the Pt ring of the RRDE. A 0.05 M H_2SO_4 aqueous solution was used as electrolyte, which was prepared by mixing high purity H_2SO_4 (Ultrapur, 96%, Merck Millipore KGaA, Germany) and ultra-pure water (18.2 MΩ cm at 20 °C, Merck Millipore KGaA, Germany). High purity Ar and H_2 (6.0-grade, Westfalen AG) were used to purge the electrolyte.

Before each measurement, the Au working electrode disk was removed from the RRDE shaft and was polished with 0.3 μm alumina polishing suspension (Buhler AG) and then sonicated in ultrapure water for several times. The catalyst ink suspension was prepared using the as-received or the partially reduced IrO_2/TiO_2 catalyst powders after the TGA experiments, ultrapure water, and Nafion® ionomer solution (5 wt.% ionomer in mixture of lower aliphatic alcohols and water, Sigma Aldrich). The ink composition was adjusted to achieve 0.98 $mg_{Ir} ml^{-1}_{ink}$ and 2 wt.% ionomer content in the final dried coating consisting of catalyst and ionomer (note: the Ir content of the partially reduced IrO_2/TiO_2 powders after the TGA experiments was re-calculated based on their mass loss during the TGA experiments). The suspension was sonicated for 30 min in a sonication bath (Elmasonic S 30 H, Elma Schmidbauer GmbH) in order to achieve a homogenous ink. The temperature of the bath was maintained below 35 °C in order to prevent solvent evaporation. Finally, 20 μl of the prepared ink was drop-casted on the polished and cleaned Au working electrode, resulting in a catalyst loading of 0.1 $mg_{Ir} cm^{-2}_{disk}$.

All the RDE measurements (using the RRDE assembly) were performed using an Autolab potentiostat (PGSTAT302N, Metrohm AG) and a rotator (Pine Research Instrumentation). The electrode rotation rate was fixed at 2500 rounds per minute (RPM) and the electrolyte temperature was maintained at room temperature during the electrochemical measurements. Freshly coated working electrodes were dipped in Ar-saturated electrolyte and the uncompensated solution resistance between the reference and working electrode was determined by electrochemical impedance spectroscopy (EIS) from 100 kHz to 100 Hz at open circuit voltage (OCV). Then, cyclic voltammetry (CV) was performed between 0.05–1.35 V_{RHE} with 20 mVs^{-1} scan rate for 10 cycles (the CVs were started with a positive going scan from OCP to 1.35 V_{RHE} followed by 10 cycles in 0.05–1.35 V_{RHE}, see Fig. A·2), in order to record the characteristic voltammetry behavior of the as-received or the partially reduced IrO_2/TiO_2 catalyst powders in this potential range as well as to make sure of the physical stability of the coatings on Au working electrode disk during the experiments. After that, an OER polarization curve was recorded by collecting a CV between 1.2–1.57 V_{RHE} with 20 mVs^{-1} scan rate where only the very first positive-going scan is used for evaluations; during both types of measurements, the electrolyte was purged by bubbling argon in the electrolyte.

Membrane electrode assembly (MEA) preparation and cell assembly.—The stability of IrO_2 under the OCV condition of a PEMFC anode was investigated using a 5 cm^2 single-cell in a self-designed flow field hardware[35] and a G60 fuel cell test station (Greenlight Innovation Corp., Canada). These MEAs had an IrO_2/TiO_2 loading of 2.0 $mg_{Ir} cm^{-2}_{MEA}$ at the anode (no platinum was used at the anode) and platinum supported on Vulcan XC72 carbon (45.8 wt.% Pt/C, TEC10V50E, Tanaka, Japan) with 0.4 $mg_{Pt} cm^{-2}_{MEA}$ loading at the cathode, hot-pressed onto a Nafion® 212 membrane (50 μm thick, from Quintech, Germany). The ionomer content of the electrodes was 12 wt.% on the anode and corresponded to an ionomer/carbon mass ratio of 0.65/1 on the cathode, using a Nafion ionomer solution (20 wt.% ionomer, D2021 from IonPower, USA). More details on the ink composition and the decal transfer to produce the catalyst coated membranes can be found in our previous study.[31] The gas diffusion layer (GDL) used for this experiment was H14C7 (Freudenberg & Co. KG, Germany), and the cell was sealed with PTFE coated fiberglass (Fiberflon, Fiberflon GmbH & Co. KG, Germany) to achieve 20% GDL compression.

The SUSD cycling and the CRT measurements were conducted using a 38 cm^2 single cell. The MEAs for these experiments were prepared using platinum supported on Vulcan carbon (50 wt.% Pt/C) with 0.3 $mg_{Pt} cm^{-2}_{MEA}$ loading at the cathode and platinum supported on graphitized Vulcan carbon (20 wt.% Pt/C) with 0.05 $mg_{Pt} cm^{-2}_{MEA}$ loading at the anode. Mitigated anode electrodes were prepared by mixing the as-received IrO_2/TiO_2 catalyst with the aforementioned Pt/C anode catalyst to achieve a loading of 0.05 $mg_{Pt} cm^{-2}_{MEA}$ + 0.05 $mg_{Ir} cm^{-2}_{MEA}$ (Pt:Ir ratio of 1:1). For simplicity, the MEAs containing the non-mitigated anode (i.e., Pt/C only) and the mitigated anode (Pt/C + IrO_2/TiO_2) will further on be referred to as "non-mitigated MEA" and "mitigated MEA," respectively. Catalyst layers were prepared with a high equivalent weight ionomer and an ionomer:carbon ratio of 0.65:1. The MEAs were prepared by decal transfer method on 18 μm thick membranes. In this case, the Freudenberg gas diffusion layer H14C10 was used, and the cell was sealed with PTFE-coated fiberglass to achieve 10% GDL compression.

Electrochemical measurements of the MEAs.—The stability of crystalline IrO_2 under the OCV condition of a PEMFC anode was

investigated in a 5 cm^2 single-cell using 2000 nccm flow of fully humidified H_2 (anode) and 5000 nccm flow of fully humidified air (cathode) at 80 °C and 170 kPa_{abs} cell pressure; nccm refers to a volumetric flow rate in units of cm^3min^{-1}, referenced to a pressure of 101.3 kPa and a temperature of 0 °C. The cell was kept under these conditions at the OCV for an overall duration of 3 h (pre-conditioning of the MEA was not done prior to this experiment). As soon as H_2 is introduced into the anode at 80 °C, metallic Ir sites begin to form on the surface of the catalyst due to the reduction of IrO_2 by H_2 through Eq. 2. Since the hydrogen oxidation reaction and hydrogen evolution reaction (HOR/HER) activities on iridium are very high,[36] the metallic Ir sites on the catalyst surface initiate an open circuit potential of the anode electrode of ~0 V vs RHE and an open circuit potential of the cathode electrode of ~0.90–0.95 V vs RHE (corresponding to the OCV of a H_2/air cell) throughout the entire 3 h of this OCV experiment. Every half an hour, cyclic voltammograms (CVs) of the anode (serving as working electrode) at ambient pressure and 40 °C were recorded using a Gamry potentiostat (Reference3000, Gamry Instruments, USA), applying a scan rate of 150 mVs^{-1} in the potential range of 0.07–1.00 V. For this, fully humidified N_2 was fed to the anode (5 nccm) and fully humidified 5 vol.% H_2/Ar to the cathode electrode (500 nccm; serving as the counter and reference electrode); an extended N_2 purge of the anode humidifier was conducted before recording the CVs.

Prior to the SUSD cycling and CRT experiments using the 38 cm^2 single-cells, the cells were conditioned under H_2/air for 8 h at 1 Acm^{-2}_{MEA} at 80 °C, an outlet pressure of 150 kPa_{abs}, and 100% relative humidity (RH). After conditioning, an H_2/air polarization curve was recorded at 80 °C and 100% RH with an outlet pressure of 150 kPa_{abs} and controlled H_2/air stoichiometries of 1.5/2. Polarization curves were recorded in galvanostatic mode, with 5 min hold at each current.

SUSD cycling was performed according to the US DRIVE Fuel Cell Technical Team Roadmap protocol at 35 °C, ambient cell pressure, and a constant cathode air flow rate corresponding to a stoichiometry of 2 at 1.0 Acm^{-2}_{MEA}.[1] A single SUSD cycle consists of five steps: i) operating the cell in fuel cell mode at 0.4 Acm^{-2}_{MEA} and 100% RH for 60 s, with an anode H_2 flow corresponding to a stoichiometry of 1.2; ii) setting the anode gas flow and the current to 0, and holding the resulting OCV for 10 s (pre-shutdown step); iii) introducing dry air to the anode compartment at a flow rate that corresponds to a residence time of 0.3 s (shutdown step); iv) setting the air flow rate in the anode to a flow corresponding to a stoichiometry of 1 at 0.1 Acm^{-2}_{MEA} for 55 s (idle step); and, finally, v) introducing fully humidified H_2 to the anode compartment at a flow rate corresponding to a stoichiometry of 1.2 at 1.0 Acm^{-2}_{MEA} (corresponding to a residence time of 0.3 s) and keeping the cell at OCV for 10 s (start-up step). H_2/air polarization curves at 80 °C (100% RH, 150 kPa_{abs}, H_2/air stoichiometries of 1.5/2.) were recorded after different SUSD cycling intervals, and the potential that corresponds to 1.2 Acm^{-2}_{MEA} was taken to compare the performance loss of MEAs upon SUSD cycling as shown in Fig. 6a.

CRTs were carried out at 80 °C and 100% RH with a gas outlet pressure of 150 kPa_{abs}. The CRT was initiated by switching the anode gas feed from H_2 to N_2 (both at 166 nccm) while flowing air in the cathode (333 nccm) and then drawing a constant current of 0.2 Acm^{-2}_{MEA}. As a result of fuel starvation in the anode, the cell potential rapidly drops to negative values in the beginning of the CRT; the end-of-life (EOL) criterion was defined as the time once the potential reached −1.5 V.

Thermogravimetric analysis (TGA).—Thermogravimetric analysis (TGA) of the as-received IrO_2/TiO_2 catalyst powder was performed by a Mettler Toledo TGA/DSC 1 instrument. ~10 mg IrO_2/TiO_2 raw powder was weighed into a sapphire crucible (volume 70 μl) closed with a perforated sapphire lid and directly inserted into the TGA furnace. All the gases used in TGA experiments were 5.0-grade and supplied by Westfalen AG. Ar (20 $mlmin^{-1}$) was used as the cell carrier gas in addition to the reactive gases during all TGA experiment steps. Each TGA experiment was composed of two main steps: i) an initial in situ drying/cleaning step in oxidative atmosphere (mass profiles of this step are not shown in the figures) and ii) a subsequent metal oxide reduction step in reductive atmosphere.

The in situ drying/cleaning step was used in order to desorb all the adsorbed water and to oxidatively remove organic molecules from the surface of the as-received catalyst powder, so that the mass losses during the subsequent reduction step are only due to the reduction of IrO_2. The procedure of the in situ drying/cleaning step was as follows: flushing the TGA furnace with Ar (100 $mlmin^{-1}$) for 5 min at 25 °C, ramping the temperature from 25 to 200 °C (10 $Kmin^{-1}$) in O_2 (100 $mlmin^{-1}$), holding the temperature at 200 °C for 10 min in O_2 (100 $mlmin^{-1}$), cooling down the furnace from 200 to 25 °C (−10 $Kmin^{-1}$) in O_2 (100 $mlmin^{-1}$), and finally purging the TGA furnace with Ar (100 $mlmin^{-1}$) for 5 min at 25 °C. Since the as-received IrO_2/TiO_2 catalyst is already heat-treated in air atmosphere at a temperature of ~ 400 °C (as stated in the patent),[30] the drying/cleaning step at 200 °C in O_2 at the beginning of each TGA experiment is not expected to have a significant influence on the as-received catalyst's physical/chemical properties (surface area, particle size, oxidation state, etc.).

After the initial drying/cleaning step, the metal oxide reduction step was carried out in two different modes: i) a temperature ramp mode and ii) an isothermal mode. During the temperature ramp experiment, the temperature was ramped from 25 to 500 °C with different heating rates (1, 2.5, 5, and 10 $Kmin^{-1}$) while supplying 5 vol.%. H_2/Ar (40 $mlmin^{-1}$), which was followed by cooling the furnace from 500 to 25 °C (−20 $Kmin^{-1}$) in Ar (100 $mlmin^{-1}$). Since IrO_2 was fully reduced at T = 350 °C during the heating step under reductive atmosphere, only the mass profiles up to 350 °C are shown in the graphs. The isothermal reduction experiments were carried out by heating the TGA furnace from 25 °C to a given target temperature (80, 100, 120, 160, or 240 °C) with a heating rate of 5 $Kmin^{-1}$ in Ar (100 $mlmin^{-1}$), followed by switching the gas supply from Ar to 5 vol.% H_2/Ar (40 $mlmin^{-1}$) and keeping the furnace at the chosen target temperature for 60 min. After this, the furnace was cooled down to 25 °C (−20 $Kmin^{-1}$) in Ar (100 $mlmin^{-1}$). Since IrO_2 reduction by H_2 occurs only during the 60 min holding temperature period, only the mass profile of this period of the entire experiment is shown in the graphs. For the extended isothermal reduction experiment in Fig. 5a, the experimental procedure was identical, except that different longer holding times under reductive conditions at the target temperature of 80 °C were applied. It should be noted that during all the IrO_2 reduction steps in TGA experiments, the effective H_2 concentration was 3.3 vol.% H_2/Ar, since in addition to the 40 $mlmin^{-1}$ 5 vol.% H_2/Ar an extra 20 $mlmin^{-1}$ flow of Ar as cell carrier gas was supplied.

IrO_2 reduction kinetics analysis.—The kinetic analysis of the TGA data was performed based on an isoconversional method to determine the Arrhenius activation energy of the IrO_2 reduction step. In this study, we used the Flynn-Wall-Ozawa (FWO) integral method, based on the procedure described in ASTM E1641–16.[37,38] This test method is based on the general rate equation derived from Arrhenius equation:

$$\frac{d\alpha}{dt} = A \cdot f_{(\alpha)} \cdot \exp\left(\frac{-E_a}{RT}\right) \quad [5]$$

where α is the reaction extent (fraction of IrO_2 reduced to Ir), t is time (min), A is pre-exponential factor, $f_{(\alpha)}$ is the reaction kinetic model, E_a is the activation energy ($Jmol^{-1}$), R is the gas constant (8.314 $Jmol^{-1}K^{-1}$), and T is the absolute temperature (in K). By applying a constant heating rate β (in $Kmin^{-1}$), Eq. 5 can be

rewritten as:

$$\frac{d\alpha}{dT} = \frac{A}{\beta}\cdot f_{(\alpha)}\cdot\exp\left(\frac{-E_a}{RT}\right) \quad [6]$$

Equation 6 can then be solved based on the FWO method for a given constant α to determine the activation energy:

$$Ln(\beta) = \ln\left(\frac{A\cdot E_a}{R\cdot g_{(\alpha)}}\right) - 5.523 - 1.053\cdot\frac{E_a}{RT} \quad [7]$$

where $g_{(\alpha)}$ is the integral form of the kinetic model ($f_{(\alpha)}$). According to Eq. 7, the activation energy at α = constant can thus be calculated by a linear regression of ln(β) vs 1/T, where T are the temperatures at which the chosen constant α is reached at different heating rates β (in this study, heating rates of 1, 2.5, 5, and 10 Kmin^{-1} were used). This analysis can be performed for different constant α values, yielding the corresponding activation energies E_a vs α. It has to be noted that Eq. 7 is valid for $20 < \frac{Ea}{R\cdot Tc} < 60$ values, where T_c is the temperature corresponding to the chosen α = constant value obtained for the TGA curve with a heating rate that is closest to the midpoint of the experimental heating rates (i.e., $\beta = 5$ Kmin^{-1} in this study). For $\frac{Ea}{R\cdot Tc}$ values outside this range, Flynn and Wall suggested corrections to determine accurate E_a values.[37] However, all the E_a values in this study fall within the $20 < \frac{Ea}{R\cdot Tc} < 60$ range, so that Eq. 7 is valid for calculating the E_a values.

Other analytical methods.—X-ray photoelectron spectroscopy (XPS) was performed on a Kratos Axis Supra spectrometer using monochromatic Al K_α radiation at an energy of 1486.6 eV. The spectra were recorded at a total X-ray source power of 225 W (15 kV and 15 mA current). For XPS measurements, as-received IrO_2/TiO_2 catalyst powder and catalyst powders after partial reduction in TGA experiments were drop-casted on a copper tape placed on a stainless steel sample holder (in floating mode, where the sample holder was electrically insulated from the copper tape), and then outgassed overnight in the ultrahigh vacuum (UHV) sample-introduction chamber to remove moisture and contaminants, so that the pressure in the analysis chamber during the XPS data acquisition remained below $1.0 \cdot 10^{-8}$ Torr. For XPS measurements on SUSD-cycled and as-prepared MEAs, the MEA samples were cut into small pieces ($\sim 5 \times 5$ mm) and attached to a self-adhesive copper tape (the electrode to be analyzed facing up) that in turn was attached to a stainless steel sample holder (in floating mode). Prior to inserting the MEA samples into the UHV sample introduction chamber, they were outgassed for 24 h in a vacuum oven at 80 °C.

High-resolution Ir 4 f and Pt 4 f spectra were collected using a step size of 0.05 eV, 0.6 s/step, and a pass energy of 20 eV; the shown spectra represent the average of 10 individual spectra. All binding energy values are corrected using the adventitious carbon signal (C 1 s = 284.8 eV). The XPS data analysis was performed using the Casa XPS software. A Shirley function was used as background. As it is reported that Ir 4 f spectra exhibit a distinct asymmetric line shape,[39,40] a Functional Lorentzian line shape was used for metallic iridium and for iridium oxides, with the parameters set to LF (0.6, 1, 150, 300) and LF (0.3, 1.5, 25, 150), respectively. The fits of the doublets of Ir 4f7/2 and Ir 4f5/2 were fixed to have the same FWHM (full width at half maximum) and to have a (4f7/2)/(4f5/2) peak area ratio of 4:3.

X-ray diffraction was performed using a Stadi P instrument (Stoe & Cie GmbH, Germany) with Cu $K_{\alpha 1}$ radiation (λ = 1.54059 Å, 50 kV, 30 mA, Ge(111) monochromatized) and a Mythen 1 K areal detector (Dectris Ltd., Switzerland) in transmission mode. About 5 mg of each powder sample was smoothly spread onto a scotch tape and placed in the center of the sample holder hole. The XRD patterns were recorded in the 2θ range of 20°–90° with a step size of 0.015° and a hold time of 0.8 s per step.

Results and Discussion

To our knowledge, the reduction of IrO_2 in a H_2-containing atmosphere has not been considered when using this material as an anode co-catalyst for mitigating cell reversal damages in PEMFCs; recent data, however, showed that IrO_2 can be partially reduced to metallic Ir when subjecting an IrO_2/TiO_2 anode catalyst in a PEM water electrolyzer to cross-over hydrogen at OCV and 80 °C.[24,29] In the following, a mechanistic understanding of IrO_2 reduction in H_2–containing atmospheres is provided. Following this, the long-term stability of IrO_2 is evaluated in an isothermal condition at a temperature of 80 °C in a H_2-containing atmosphere (simulated PEMFC anode reductive environment). Lastly, the effect of partial reduction of IrO_2 in a PEMFC anode condition when used as an anode co-catalyst is investigated on the long-term durability of PEMFCs.

Fundamental aspects of IrO_2 reduction in H_2-containing atmospheres.—TGA is a well-established technique that can be used to unveil the underlying mechanism of metal oxide reduction even for complex multi-step reactions.[41–43] Figure 2a shows the TGA temperature ramp curves of the as-received IrO_2/TiO_2 catalyst in 3.3 vol.% H_2/Ar carried out at four different heating rates (β = 1, 2.5, 5, and 10 Kmin^{-1}). The TGA curves show the onset of a mass loss at temperatures of ~85 °C–110 °C, depending on the heating rate. The mass loss vs temperature curves are approaching the theoretical mass loss that would be expected for the full reduction of IrO_2 in the IrO_2/TiO_2 catalyst to metallic Ir (i.e., a loss of 12.5 wt.%, see experimental section) at ~350 °C. Since TiO_2 is completely inert to reduction by H_2 at this temperature range,[44–46] the TGA curves imply that the entire mass loss between 80 °C–350 °C corresponds to the reduction of IrO_2 in the IrO_2/TiO_2 catalyst through Eq. 2. The agreement between the experimental mass loss and that predicted by Eq. 2 indicates that iridium in the here used IrO_2/TiO_2 catalyst is, at least predominantly, in the form of iridium (IV) oxide. It should be noted that desorption of adsorbed water or any other organic residues on the surface of the catalyst does not contribute to the observed mass loss in the initial stage due to the in situ drying/cleaning step prior to the TGA measurement under reducing conditions (see experimental section).

As only IrO_2 can be reduced under these conditions and as the weight loss up to 500 °C (data only shown up to 350 °C in Fig. 2a) corresponds to the complete reduction of IrO_2 to Ir, the mass loss plotted on the left y-axis in Fig. 2a can be converted to the fraction of IrO_2 reduced to metallic Ir (α), marked by the right y-axis. From this it can be seen that the TGA curves are composed of an initially fast mass loss with increasing temperature for $\alpha < 60\%$, followed by a much more gradual mass loss with temperature for α ranging between 60%–100%. This might suggest that the kinetics of the IrO_2 reduction in the IrO_2/TiO_2 catalyst follows multi-step reaction kinetics, characterized by an initially high rate that gradually slows down as the reduction reaction extent proceeds to $\alpha > 60\%$. In order to get better insights into the IrO_2 reduction kinetics for the IrO_2/TiO_2 catalyst, the Flynn-Wall-Ozawa (FWO) method described in the experimental section is used to perform a kinetic analysis and to calculate the activation energy for the reduction of the IrO_2 phase of the IrO_2/TiO_2 catalyst. The FWO method is a kinetic model-independent analysis method, which can provide the activation energy at each reaction extent α, which is also suitable when several reaction steps are occurring simultaneously and when the activation energy varies with the reaction extent α.[47,48] Figure 2b shows the linear regressions of the Ln(β) vs 1/T points which are collected from the TGA curves in Fig. 2a at constant reaction extents α, selected between α = 5%–90%. The horizontal and vertical black

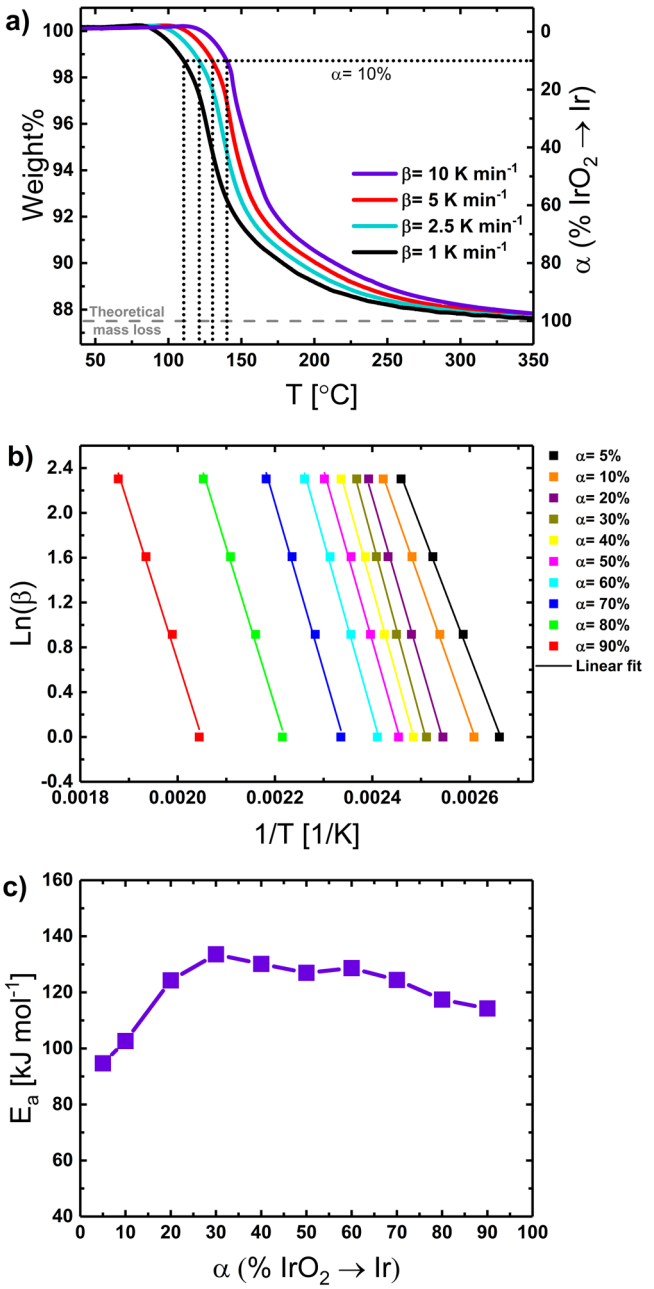

Figure 2. (**a**) TGA temperature ramp experiments with the as-received IrO_2/TiO_2 catalyst power under 3.3 vol.% H_2/Ar at heating rates of 1, 2.5, 5, and 10 $Kmin^{-1}$ (following the drying/cleaning step; see experimental section). The left *y*-axis represents the weight% mass loss of the IrO_2/TiO_2 catalyst vs temperature, while the fraction of the IrO_2 phase that is reduced to metallic Ir (α) is given on the right *y*-axis. The gray horizontal dashed line marks the theoretical mass loss (12.5 wt.%) of the IrO_2/TiO_2 catalyst upon the complete reduction of the IrO_2 phase by H_2 to metallic Ir (see Eq. 2). The black horizontal and vertical dotted lines illustrate the data that are used for the analysis in b) for a reaction extent of $\alpha = 10\%$. (**b**) Linear regression of $Ln(\beta)$ vs 1/T points collected from a) at constant α values selected between 5%–90%. The squares represent the data points at different constant α values, and the solid lines are the linear regression fits of the data points at each set of α values. (**c**) Plot of activation energy vs α for the reduction of the IrO_2 phase of the IrO_2/TiO_2 catalyst, calculated based on FWO method (Eq. 7), using the regression line slopes in b).

dotted lines in Fig. 2a exemplarily illustrate the data collection at $\alpha = 10\%$. All of the regression lines in Fig. 2b fit to the data points with $R^2 > 0.99$. The activation energy at each α value is calculated from Eq. 7, using the slopes of the fitted lines in Fig. 2b, and the thus determined activation energies E_a vs α are plotted in Fig. 2c. It can be seen in Fig. 2c that the activation energy of IrO_2/TiO_2 reduction is ~95 and ~105 $kJmol^{-1}$ for low reaction extents α of 5% and 10%, respectively; at α ranging between 20%–70% the activation energy is ~130 ± 5 $kJmol^{-1}$, then decreasing to ~115 $kJmol^{-1}$ as α reaches 90%. Interestingly, the clearly lower activation energies up to $\alpha = 10\%$ corresponds to the reduction of approximately one monolayer of the IrO_2 phase (see above estimates), suggesting that the outermost monolayer can be reduced more easily than the bulk of the IrO_2 phase. This has also already been suggested for the same catalyst based on differential scanning calorimetry data.[24] One possible explanation for the apparently more facile reduction of the outermost surface layer(s) of the iridium oxide phase would be that this near-surface region is amorphous, as amorphous iridium oxide was shown to be more readily reducible by H_2 (at temperatures of ~80 °C) compared to crystalline rutile type IrO_2.[40,49]

In summary, the above data suggest that the one or two outermost monolayers of the IrO_2 phase of the catalyst consist of an iridium oxide phase that on account of OH surface terminations and/or surface imperfections is amorphous (furtheron referred to A-IrO_x), and that has a lower activation energy for reduction to metallic Ir by H_2. As the reduction reaction proceeds further into to the sub-surface layers of the IrO_2 phase, the reduction of more stable crystalline iridium oxide (C-IrO_2) in the bulk of the catalyst starts to take place, indicated by a higher apparent activation energy for mixtures of A-IrO_x and C-IrO_2. The initially fast mass loss with increasing temperature for $\alpha < 60\%$ (see Fig. 2a) suggests that the A-IrO_x species are mainly reduced at $\alpha < 60\%$; on the other hand, the more gradual mass loss for α ranging between 60%–100% suggests that the innermost IrO_2 phase becomes more and more crystalline, i.e., less reducible.

Although TGA temperature ramp experiments are a useful method to compare the temperature range for the reduction of different IrO_2 catalysts in an H_2-containing atmosphere, they do not provide sufficient information to project the long-term stability of the iridium oxide phase under the isothermal working condition of a fuel cell anode. Therefore, TGA isothermal experiments were designed to study the reduction behavior of the IrO_2 phase of the IrO_2/TiO_2 catalyst at different temperatures of 80 °C–240 °C over a period of 1 h. The mass losses over the course of this isothermal reduction step in 3.3 vol.% H_2/Ar (marked here as time = 0) at a given target temperature are plotted in Fig. 3a, whereby the mass profiles for the initial temperature ramp from 25 °C to the target temperature that is performed in Ar atmosphere are not shown in Fig. 3a. Looking at the entire 1 h time span of the isotherms, it becomes clear that the reduction of the IrO_2 phase occurs at temperatures as low as 80 °C, although the reaction is much faster at higher temperatures such as 160 °C or 240 °C, where respectively ~65% or ~85% of the iridium oxide phase are reduced within only ~11 min. An interesting feature is the initial mass gain of ~0.1–0.2 wt.% when the gas is switched from Ar to 3.3 vol.% H_2/Ar at the targeted temperature, as shown in the magnified isotherms in Fig. 3b. This mass gain is likely due to the adsorption of hydrogen on the iridium oxide surface of the IrO_2/TiO_2 catalyst, as this is reported to be one of the initial steps during the reduction of a metal oxide by H_2 gas.[40,49,50] Assuming that each of the surface oxygens in the outermost monolayer of the iridium oxide phase were to bond to one H-atom, the molar H-uptake would be two times the moles of IrO_2 in the outermost surface layer ($n_{IrO2(ML)} = 3.83 \cdot 10^{-4} mol_{IrO2}\, g^{-1}_{IrO2/TiO2}$, see Eq. 3), corresponding to $7.66 \cdot 10^{-4}\ mol_H\, g^{-1}_{IrO2/TiO2}$ or ~0.08 wt.%, which, within the error of measurement, is in the same range as the mass gain observed in Fig. 3b.

Next we will examine the surface chemistry and the structure of the IrO_2/TiO_2 catalyst samples after the TGA experiments under 3.3 vol.% H_2/Ar in order to identify the nature of reduction products. Figure 4a and b show the XPS Ir4f spectra and XRD patterns, respectively, of the as-received IrO_2/TiO_2 catalyst and of several (partially) reduced IrO_2/TiO_2 powders after the TGA experiments.

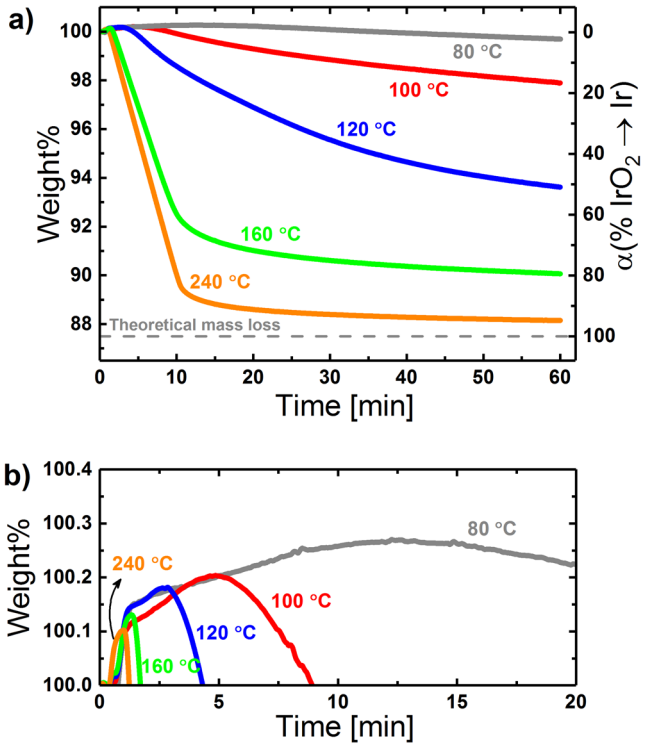

Figure 3. (**a**) Isothermal TGA experiments on the reduction of the iridium oxide phase of the IrO_2/TiO_2 catalyst in 3.3 vol.% H_2/Ar at 80, 100, 120, 160, and 240 °C (following the drying/cleaning step; see experimental section). The left *y*-axis represents the mass loss in wt.% of the IrO_2/TiO_2 catalyst vs temperature, while the fraction of the IrO_2 phase that is reduced to metallic Ir (α) is given on the right *y*-axis. The gray horizontal dashed line marks the theoretical mass loss (12.5 wt.%) of the IrO_2/TiO_2 catalyst upon the complete reduction of the IrO_2 phase by H_2 to metallic Ir (see Eq. 2). (**b**) Magnification of the initial 20 min of a).

Table I summarizes the XPS Ir4f peak deconvolution parameters and the calculated composition of each sample based on the fitted spectra. The Ir4f XPS spectrum of the as-received IrO_2/TiO_2 catalyst (see Fig. 4a) can be fitted to C-IrO_2 and A-IrO_x components, yielding a composition ratio of A-IrO_x:C-IrO_2 = 41:59 (for the fitting procedure, see experimental section), with no contributions from metallic iridium being detected. The XRD pattern of the as-received IrO_2/TiO_2 catalyst (see Fig. 4b) is composed of broad crystallite reflections of rutile C-IrO_2 from the crystalline portion of the iridium oxide phase (main reflections marked by the red dotted lines) and the anatase TiO_2 (main reflections marked by the green dotted lines) from the TiO_2 support of the catalyst. Next, we will examine the XPS and XRD data for the IrO_2/TiO_2 catalyst after the 1 h isothermal TGA experiment at 120 °C (see blue line in Fig. 3a). The clear detection of metallic Ir in the XPS spectrum of the thus treated IrO_2/TiO_2 catalyst confirms that the observed mass loss in Fig. 3a corresponds to the partial reduction of IrO_2 by H_2 through Eq. 2, with metallic Ir being the product of this reaction. The XRD pattern of this sample shows that the metallic Ir forms crystalline domains, indicated by the unique reflection at $2\theta \approx 89°$ (see right-most gray dotted line in Fig. 4b). In addition, strong diffractions for C-IrO_2 and anatase TiO_2 are still observed, so that the sample is composed of all three crystalline phases. Based on the XPS analysis (Table I), the surface composition of the sample with respect to metallic iridium and the crystalline and amorphous iridium oxide phases corresponds to Ir:C-IrO_2:A-IrO_x ≈ 42:47:11, indicating that the overall fraction of amorphous iridium oxide (∼11%) in the near-surface region has greatly decreased compared to the as-received IrO_2/TiO_2 sample (∼41%), which is also reflected by the much lower A-IrO_x:C-IrO_2 ratio in the reduced sample (11/47 = 0.23/1) compared to the as-received sample (41/59 = 0.69/1). This observation is in line with the reaction mechanism proposed in the context of the discussion of Fig. 2, namely that A-IrO_x is being reduced predominantly in the beginning of the reduction reaction. Increasing the isothermal reaction temperature to 240 °C or ramping the temperature from 25 to 500 °C leads to the full reduction of iridium oxide to metallic Ir, which can be seen clearly by an inspection of the XPS data (Fig. 4a) and the XPS peak fitting results (Table I) as well as by the XRD data (Fig. 4b), where all of the features unique to C-IrO_2 have disappeared. The sharper diffraction lines for the sample ramped to 500 °C is indicative of more pronounced growth of the metallic Ir domains at this higher final reduction temperature.

Overall, both TGA temperature ramp and isothermal experiments can in principle be used to study the reduction of IrO_2 in H_2-containing atmospheres, but the choice of the method depends on the question to be answered. The temperature ramp is a quick experiment for comparing the temperature stability window of different catalysts, while the time consuming isothermal experiment might be more useful when trying to get information at conditions that more closely reflect those in real applications. The latter point will be demonstrated in the next section, showing that isothermal TGA experiments can be used to project the behavior of an IrO_2/TiO_2 catalyst under the conditions of a PEMFC anode.

IrO_2 reduction in a simulated PEMFC anode reductive environment.—When using IrO_2 as an anode co-catalyst in PEMFCs, it is crucial to know the effect of the strongly reducing conditions in the hydrogen anode (∼1 bar H_2, 80 °C, and ∼0 V vs RHE) on the chemical stability of IrO_2. While probing the stability of IrO_2 directly in the anode of a PEMFC is possible, this approach has several disadvantages: i) it requires the time-consuming preparation/optimization of electrodes and their integration in membrane electrode assemblies (MEAs); ii) MEA preparation requires a considerable amount of catalyst (at least a few hundred milligrams), which often is a significant hurdle when exploring new catalysts synthesized by different methods; iii) the electrochemical characterization methods performed in a fuel cell are mainly sensitive to the chemical changes in the near-surface regions of a catalyst, and the analysis of bulk phases (e.g., via XRD) requires cumbersome post-mortem analysis; and, iv) MEA characterization in a fuel cell introduces additional complexity due to multiple reactions occurring in parallel. On the other hand, isothermal TGA experiments can be designed to simulate the reductive environment of PEMFC anodes, whereby no sample preparation is required, only a few milligrams of a sample are needed, and the observed sample mass loss can be directly and quantitatively correlated to the amount of reduced IrO_2 (surface and bulk). Therefore, long-term (up to 24 h) isothermal TGA experiments have been performed at 80 °C to investigate the stability of the iridium oxide phase of the IrO_2/TiO_2 catalyst in the presence of hydrogen, and the results are shown in Fig. 5a. To aid the interpretation of the data, the IrO_2/TiO_2 catalyst is assumed to have a core–shell morphology, with the surface of the TiO_2 support covered completely by IrO_2 particles or by an IrO_2 film (the latter is sketched in Fig. 5c). Nevertheless, Fig. 5c is a simplified sketch of the IrO_2/TiO_2 catalyst that is used here. All the assumptions regarding the calculation of the monolayer of IrO_2 (ML_{IrO_2}) on the IrO_2/TiO_2 catalyst surface in the experimental section are made while being based on a morphology that TiO_2 support is completely covered by IrO_2 particles; that is similar to Fig. A·1, inset.

The IrO_2/TiO_2 catalyst mass loss vs time for the long-term isothermal TGA experiment (Fig. 5a) reveals that a continuous IrO_2 reduction occurs over the entire course of the experiment, not showing any plateau in the mass loss even after 24 h. Based on our estimate (see experimental section) for the mass loss or the reaction extent α which correspond to the reduction of a monolayer of the iridium oxide phase (1 ML_{IrO2} amounts to ∼1.25 wt.% mass loss or to $\alpha \approx 10\%$), the estimated numbers of IrO_2 monolayers that are

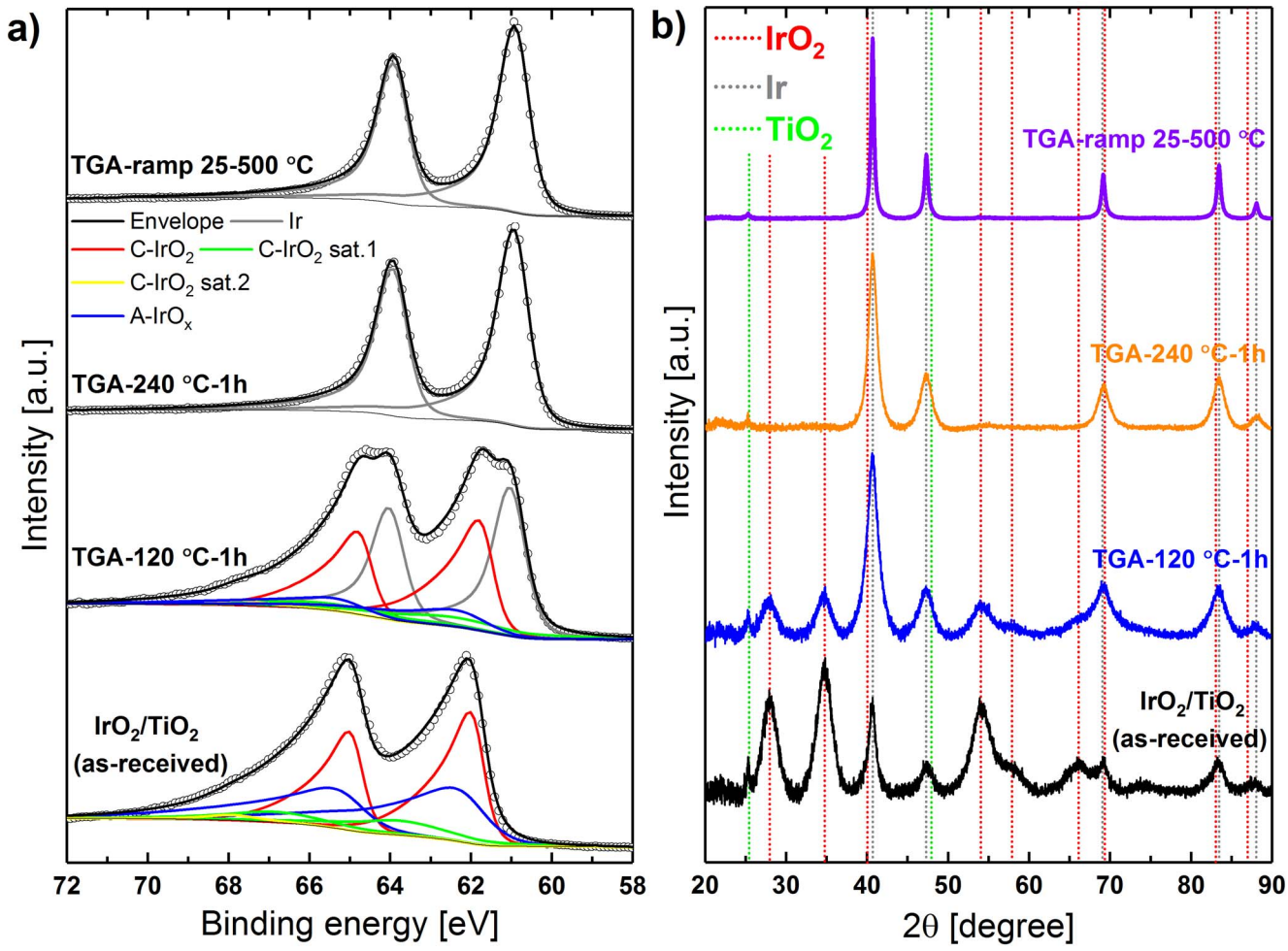

Figure 4. Post characterization of the as-received IrO_2/TiO_2 catalyst and of (partially) reduced IrO_2/TiO_2 catalyst powders after the TGA experiments in Fig. 3 by: (**a**) XPS Ir4f spectra and (**b**) XRD. *Sample notations:* TGA-120 °C-1h and TGA-240 °C-1h refer to the materials obtained after the 1 h isothermal TGA experiments (see Fig. 3a) and TGA-ramp 25 °C–500 °C refers to the material obtained after the TGA temperature ramp experiment at a heating rate of $\beta = 5\ Kmin^{-1}$ (see Fig. 2a). Detailed peak deconvolution parameters and the ratios between different Ir species in (a) can be found in Table I. The vertical dotted lines in (b) are the main reference crystalline peak positions for metallic Ir (gray), rutile C-IrO_2 (red), and anatase TiO_2 (green).

reduced to metallic iridium are marked by the orange dotted lines in Fig. 5a. This analysis implies that the reduction of the iridium oxide phase of the IrO_2/TiO_2 catalyst at 80 °C is not limited to the outermost monolayer(s) of the iridium oxide phase, but that it rather proceeds further towards its bulk; after 24 h in 3.3 vol.% H_2/Ar at 80 °C, the data suggest that more than four ML_{IrO2} equivalents of the IrO_2 phase have been reduced, corresponding to $\alpha > 40\%$.

Next, we will show that the above described surface and sub-surface reduction of the IrO_2 phase of the IrO_2/TiO_2 catalyst has a strong impact on its electrochemical behavior. For this, IrO_2/TiO_2 powder samples were subjected to different isothermal TGA intervals of 0.5, 3, 12, and 24 h (marked by the asterisks in Fig. 5a), and their electrochemical behavior was then characterized by RDE measurements and compared with that of the as-received IrO_2/TiO_2 catalyst. Figure 5b shows the CVs (first scans out of the 10 measured scans for each sample are shown, the starting positive sweeps from OCP to 1.35 V_{RHE} are removed, see Fig. A·2) of these samples in an Ar saturated 0.05 M H_2SO_4 electrolyte at a scan rate of 20 mVs^{-1}. Although the surface composition of the as-received IrO_2/TiO_2 is composed of two different IrO_2 species, namely A-IrO_x and C-IrO_2 (see Table I), the voltammetric features of this sample are resembling those of a highly crystalline and heat-treated IrO_2; this is indicative of an electrochemically stable IrO_2 phase in the as-received IrO_2/TiO_2 catalyst.[51] It can be seen that after only 0.5 h of the isothermal TGA experiment (green asterisk in Fig. 5a), the capacitive currents are increased by ~3-fold (green line) compared to those of the as-received IrO_2/TiO_2 (black line), due to the formation of sub-monolayer amounts of metallic Ir on the catalyst surface. Nevertheless, the CV features still closely resemble that of the as-received catalyst.

Further reduction of the iridium oxide phase of the IrO_2/TiO_2 catalyst, equating to the reduction of roughly 1 ML_{IrO2} (i.e., after 3 h, blue asterisk in Fig. 5a), leads to the appearance of voltammetric features for the hydrogen under-potential deposition (H_{upd}) between 0.05–0.40 V_{RHE}, characteristic of metallic polycrystalline iridium or carbon-supported iridium nanoparticles.[52,53] This suggests that the reduction of ~1 ML_{IrO2} and thus the formation of ~1 ML_{Ir} on the surface of the IrO_2/TiO_2 catalyst is sufficient to completely change its voltammetry from that corresponding to heat-treated IrO_2 to that corresponding to metallic Ir. After reducing the IrO_2/TiO_2 catalyst for longer times of 12 or 24 h, where ~3 or >4 ML_{IrO2} equivalents are reduced, the CVs reach a steady-state, indicating that the reduction of sub-surface layers of the iridium oxide phase does not further increase the H_{upd} region. This is due to the fact that H adsorption/desorption occurs only on the outermost surface of the apparently compact and dense metallic Ir phase that is formed during reduction at 80 °C. The reduction of the iridium oxide phase of the IrO_2/TiO_2 catalyst during the extended isothermal TGA experiment is schematically shown in Fig. 5c.

In order to validate that the results obtained in the isothermal TGA experiment are representative of what happens to the

Table I. XPS Ir4f peak deconvolution parameters and the calculated composition of as-received and (partially) reduced IrO_2/TiO_2 samples based on the fitted XPS Ir4f spectra in Fig. 4a. C-IrO_2 refers to crystalline IrO_2, A-IrO_x refers to amorphous iridium oxide. Details of the fitting procedure are described in the experimental section.

Sample	Peak	B.E. [eV]	FWHM [eV]	Area [%]	Composition
IrO_2/TiO_2 (as-received)	C-IrO_2 4f7/2	61.92	0.81	26.24	
	C-IrO_2 4f5/2	64.92	0.81	19.72	
	C-IrO_2 4f7/2 (sat.1)	63.80	2.91	6.83	C-IrO_2: 59%
	C-IrO_2 4f5/2 (sat.1)	66.80	2.91	4.94	A-IrO_x: 41%
	C-IrO_2 4f5/2 (sat.2)	67.90	1.53	1.32	
	A-IrO_x 4f7/2	62.20	1.79	23.38	
	A-IrO_x 4f5/2	65.20	1.79	17.57	
TGA-120 °C-1h	Ir 4f7/2	60.99	0.90	23.84	
	Ir 4f5/2	63.99	0.90	17.92	
	C-IrO_2 4f7/2	61.71	0.85	20.56	
	C-IrO_2 4f5/2	64.71	0.85	15.45	metallic Ir: 42%
	C-IrO_2 4f7/2 (sat.1)	63.5	3.6	5.61	C-IrO_2: 47%
	C-IrO_2 4f5/2 (sat.1)	66.5	3.6	4.06	A-IrO_x: 11%
	C-IrO_2 4f5/2 (sat.2)	67.71	1.57	1.04	
	A-IrO_x 4f7/2	62.21	1.8	6.63	
	A-IrO_x 4f5/2	65.21	1.8	4.98	
TGA-240 °C-1h	Ir 4f7/2	60.90	0.87	57.09	metallic Ir: 100%
	Ir 4f5/2	63.90	0.87	42.91	
TGA-ramp 25 °C–500 °C	Ir 4f7/2	60.88	0.86	57.09	metallic Ir: 100%
	Ir 4f5/2	63.88	0.86	42.91	

IrO_2/TiO_2 catalyst in a PEMFC anode, its stability was tested in an MEA. An MEA with an active area of 5 cm^2 was prepared, where IrO_2/TiO_2 was used in the anode electrode and a Pt/C catalyst was used in the cathode electrode. The MEA was held at OCV ($E_{anode} \approx 0$ V vs RHE and $E_{cathode} \approx 0.9$–0.95 V vs RHE, see experimental section) at 80 °C, with a constant flow of fully-humidified H_2 (2000 nccm) through the anode compartment pressurized at 170 kPa_{abs} (corresponding to a H_2 partial pressure of 123 kPa). Every 30 min, anode CVs were recorded at 40 °C, and were compared to the CV of the as-received IrO_2/TiO_2 catalyst (before ever flowing H_2 through the anode), as shown in Fig. 5d. The observed gradual formation of H_{upd} features of metallic Ir in Fig. 5d suggests that, similar to the TGA experiment, IrO_2 reduction upon exposure to H_2 also occurs in an MEA in a PEMFC (analogous to what was shown previously for a PEM water electrolyzer configuration[24,29]). However, the reduction kinetics of the IrO_2 phase seems to be faster in the MEA, where it takes ~2 h for the surface of the IrO_2 phase to completely convert to metallic Ir and for the CVs to reach a steady-state. This is most likely due to the higher H_2 partial pressure in the MEA experiment (P_{H2} = 123 kPa) compared to that in the TGA experiment (P_{H2} = 3.3 kPa). It has to be noted that although the CVs recorded in the MEA reach a steady state after ~2 h of OCV (see Fig. 5d), it is speculated based on the TGA results (and based on the analogy of the TGA and MEA experiments) that the reduction of the IrO_2 phase of the IrO_2/TiO_2 catalyst also proceeds to subsurface layers of IrO_2, even though the formation of bulk metallic Ir is not further traceable by measuring CVs in the MEA. It is also worth mentioning that the high iridium loading of 2.0 $mg_{Ir}cm^{-2}_{MEA}$ used in this section is not relevant for the application of IrO_2 as an anode co-catalyst in a PEMFC, and it is only used to show the instability of IrO_2 in the reductive atmosphere of a PEMFC anode. The following sections of the paper will show that a more relevant loading of 0.05 $mg_{Ir}cm^{-2}_{MEA}$ will be used in the CRT and SUSD experiments.

A more active OER catalyst facilitates the OER over the COR during cell reversal in a PEMFC, resulting in longer cell reversal tolerance times.[19,20] Measuring the OER activity of a catalyst using the RDE technique is a quick and reasonably reliable approach to predict its OER activity in an MEA.[54,55] Therefore, Fig. 5e shows the RDE-based OER polarization curves of the as-received IrO_2/TiO_2 catalyst (black line) and the catalyst after the respective isothermal TGA hold times shown in Fig. 5a. The polarization curves were recorded after 10 CVs in the potential window of 0.05–1.35 V_{RHE} in the Ar-saturated electrolyte (shown in Fig. A·2), whereby the potential that corresponds to the electrode current of 10 $mAcm^{-2}_{disk}$ is frequently taken as a measure of the OER activity.[56] It can be seen in Fig. 5e that the OER activity of the electrodes is increasing with increasing isothermal hold times at 80 °C, whereby the OER activity is improved by 38 mV after a 24 h hold time compared to the as-received IrO_2/TiO_2 catalyst. Analogous improvements of the OER activity (between 20–40 mV) were also observed when subjecting the same IrO_2/TiO_2 catalyst in the anode catalyst layer of a PEM water electrolyzer to cross-over hydrogen at OCV and 80 °C.[24,29] Based on the analysis of Figs. 5a and 5e, such OER activity improvement is directly correlated to the reduction of IrO_2 and the formation of metallic Ir in the near-surface layer of the IrO_2 phase. It is well known that the product of electrochemical oxidation of metallic Ir (furtheron referred to as E-IrO_x, denoting a highly porous, hydrated iridium oxy-hydroxide) has a substantially higher OER activity than heat-treated IrO_2,[57–59] which explains why the OER activity of the IrO_2/TiO_2 catalyst increases with increasing reduction time in Fig. 5a. The transformation of metallic Ir to E-IrO_x over the course of 10 CVs in the potential window of 0.05–1.35 V_{RHE} prior to the measurement of the OER polarization curves can be seen in Fig. A·2, where the appearance of voltammetric features in the potential range of ~0.7–1.2 V_{RHE} upon cycling is indicative of the transformation of the near-surface region metallic Ir to E-IrO_x. In fact, this feature is more prominent for the samples reduced for 12 and 24 h (Figs. A·2c and A·2d), which showed a nominal reduction of ~3 and ~4.5 ML_{IrO2}, respectively. This is due to the fact that upon cycling the electrodes between 0.05–1.35 V_{RHE}, further oxidation of sub-surface metallic Ir leads to the formation of a thicker porous E-IrO_x layer on the catalyst surface and to an incorporation of the near-surface active sites to the electrochemical processes.[60,61] This phenomenon, so called three-dimensional electrocatalysis,[59] explains the higher OER activity of the samples reduced for 12 and 24 h (reduction of ~3 and ~4.5 ML_{IrO_2} on IrO_2 surface) compared to the sample reduced for 3 h (reduction of ~1 ML_{IrO_2} on IrO_2 surface).

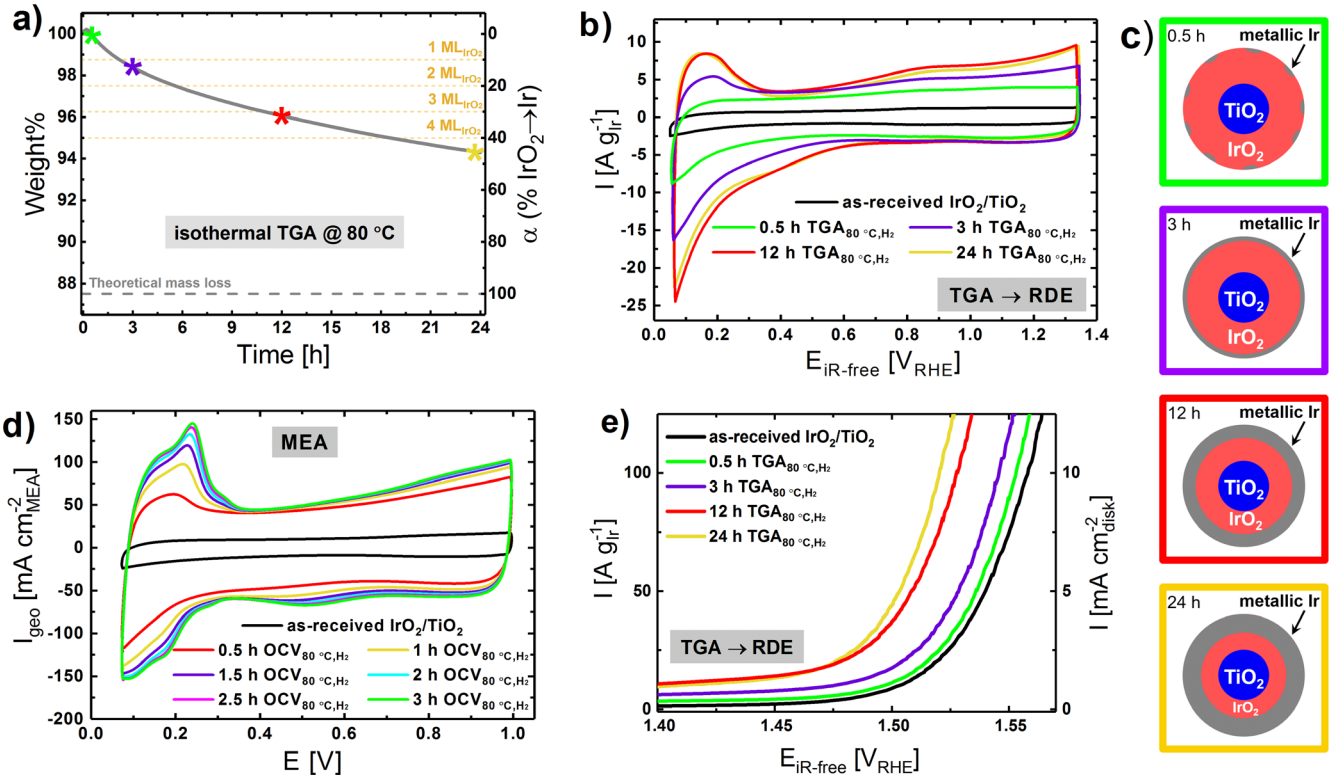

Figure 5. (**a**) Extended-time isothermal TGA experiments on the reduction of the iridium oxide phase of the IrO_2/TiO_2 catalyst in 3.3 vol.% H_2/Ar at 80 °C, aiming to simulate the PEMFC hydrogen anode reductive environment. The left *y*-axis represents the mass loss in wt.% of the IrO_2/TiO_2 catalyst vs time, while the fraction of the IrO_2 phase that is reduced to metallic Ir (α) is given on the right *y*-axis. The orange dotted lines represent the reduction of 1–4 monolayers of IrO_2 (ML_{IrO2}), whereby the reduction of 1 ML_{IrO2} corresponds to an estimated mass loss of ~1.25 wt.% or to a reaction extent of $\alpha \approx 10\%$; the gray dashed line marks the theoretical mass loss (12.5 wt.%) of the IrO_2/TiO_2 catalyst upon the full reduction of the IrO_2 phase to Ir (see experimental section). The asterisks mark the reduction times for the independently prepared samples for the electrochemical measurements in b) and e). (**b**) Cyclic voltammograms (CVs) of the as-received IrO_2/TiO_2 catalyst and of the partially reduced IrO_2/TiO_2 samples marked in a); they were recorded in an RDE configuration at room temperature between 0.05–1.35 V_{RHE} at a scan rate of 20 mVs^{-1} in Ar saturated 0.05 M H_2SO_4 (loading of 0.1 $mg_{Ir}cm^{-2}{}_{disk}$) at a rotation rate of 2500 RPM (1st cycle; all 10 cycles are shown in figure A.2). (**c**) Schematic representation of the reduction of the IrO_2/TiO_2 surface to metallic Ir during the extended-time isothermal TGA experiment in a), assuming a core/shell morphology. (**d**) CVs at 150 mVs^{-1} of the as-received IrO_2/TiO_2 catalyst incorporated as anode in a 5 cm^2 MEA (2.0 $mg_{Ir}cm^{-2}{}_{MEA}$) with a Pt/C cathode (0.4 $mg_{Pt}cm^{-2}{}_{MEA}$). The CVs, taken after a series of 30 min holds at OCV (80 °C, 170 $kPa_{abs.}$, 2000 nccm H_2 (anode)/ 5000 nccm air (cathode)), were acquired between 0.07–1.00 V at 40 °C and ambient pressure with fully-humidified N_2 (anode) and 5 vol.% H_2/Ar (cathode). (**e**) OER polarization curves of the as-received IrO_2/TiO_2 catalyst and of the partially reduced IrO_2/TiO_2 samples taken at 20 mVs^{-1} and 2500 RPM in Ar-saturated 0.05 M H_2SO_4 at room temperature (0.1 $mg_{Ir}cm^{-2}{}_{disk}$).

Based on the conclusions drawn from the TGA and RDE experiments, and their confirmation by the MEA experiments in a PEMFC, it is clear that at least the near-surface layers of the IrO_2 phase of the IrO_2/TiO_2 catalyst can be reduced to metallic Ir by H_2 under the conditions of a PEMFC anode. This formation of metallic Ir at/near the catalyst surface also alters the electrochemical properties of the catalyst, leading to a drastic increase in its OER activity. A consequence of this phenomenon is that OER catalyst testing in an RDE, where the potential is usually kept above 1 V vs RHE, can yield a vastly different OER activity from that of the same catalyst, when it is used as an anode co-catalyst in a PEMFC. For example, the OER activity of the here used IrO_2/TiO_2 catalyst (corresponding to the black line in Fig. 5e) will be much lower than its activity as a cell reversal mitigation catalyst in a PEMFC anode (more closely corresponding to the yellow line in Fig. 5e). By the same token, IrO_2 based catalysts that are made by different synthesis routes could, e.g., be predominantly amorphous (or consisting of hydrous iridium oxide) or highly crystalline, which in turn would lead to a different degree of reducibility under H_2 (the higher degree of reducibility of amorphous iridium oxide is suggested by Figs. 2 and 3). As a more easily reducible IrO_2 catalyst would be expected to have a higher OER activity, it would also be expected to show a better cell reversal mitigation performance when used as an anode co-catalyst in a PEMFC. This phenomenon might explain the occasional discrepancy observed between the OER activity of a series of catalysts measured by the RDE technique, and their performance as anode co-catalysts in cell reversal tests (CRTs) in a PEMFC (for example, compare Figs. 3a and 5a in Roh et al.,[19] and Figs. 4a and 5a in Moore et al.[20]). Therefore, the possibly different surface state of an IrO_2 based catalyst in conventional RDE based OER activity measurements vs that when used as anode co-catalyst in a PEMFC must be considered. In the next section, further consequences of the near-surface reduction of the IrO_2 phase of the IrO_2/TiO_2 catalyst when used as anode co-catalyst on PEMFC durability will be discussed.

Degradation of an IrO_2/TiO_2 anode co-catalyst by SUSD cycling.—Based on the results of the previous section it is now clear that during the normal operating conditions of a PEMFC, the IrO_2 phase of the IrO_2/TiO_2 catalyst when used as anode co-catalyst will get (partially) reduced to metallic Ir and, accordingly, its electrochemical behavior will change substantially. This phenomenon could eventually affect the stability of such an anode co-catalyst during the transient operation of a PEMFC, e.g., during SUSD and cell reversal events. In this regard, an accelerated SUSD test was performed with 38 cm^2 active area MEAs with a Pt/C catalyst in the cathode electrode and two different types of anode electrodes, namely either only with Pt/C (furtheron referred to as *non-mitigated MEA*) or with a mixture of Pt/C and the IrO_2/TiO_2 as anode co-catalyst (furtheron referred to as *mitigated MEA*). The

accelerated SUSD experiments are performed at a temperature of 35 °C, according to the US DRIVE Fuel Cell Technical Team Roadmap protocol (see experimental section), so that the strongly temperature-dependent Pt/C catalyst degradation during SUSD events is minimized[26] and any degradation that may be caused by the IrO_2/TiO_2 anode co-catalyst can be more easily determined. Figure 6a shows the cell potential profiles at a current density of 1.2 Acm^{-2}_{MEA} as a function of performed SUSD cycles, determined from H_2/air (s = 1.5/2) performance curves at 80 °C, 100% RH, and 150 $kPa_{abs,outlet}$ pressure. For the non-mitigated MEA (turquoise line/symbols in Fig. 6a), the H_2/air performance at 1.2 Acm^{-2}_{MEA} drops by ∼15 mV over the first 10 cycles and then remains roughly constant up to 100 cycles, after which it continuously decreases. The nearly constant performance over the first 100 cycles is likely due to a compensation of the SUSD losses by an activation of the Pt/C cathode catalyst caused by the positive potential excursion during the initial SUSD cycles.[62] The overall SUSD induced performance loss with an unmitigated MEA is predominantly due to carbon support corrosion at the cathode, leading to a collapse of the cathode electrode (the so-called cathode thinning) and concomitant O_2 transport losses, and to a loss of Pt surface area at the cathode.[26] It should be noted that for each SUSD cycle, the anode electrode experiences a potential cycling between ∼0–1.05 V_{RHE} upon the H_2/air_{anode} gas front passage, which also causes Pt dissolution and loss of electrochemically active surface area (ECSA) at the anode.[28] However, at least for a pure Pt/C anode, the contribution of anode ECSA loss to the overall losses caused by SUSD is negligible, due to the fast hydrogen oxidation reaction (HOR) kinetics on Pt, as long as the anode loadings are not ultra-low (i.e., not $\ll$0.05 $mg_{Pt}cm^{-2}_{MEA}$).[28]

In order to quantify the degradation rate of the non-mitigated MEA upon SUSD cycling, the H_2/air front residence time normalized SUSD degradation rate at 35 °C for the non-mitigated MEA was calculated according to Mittermeier et al.[26] Considering a potential loss of ∼80 mV over the 500 SUSD cycles (neglecting the initial activation effect of the Pt/C cathode catalyst) and the H_2/air front residence time of ∼0.3 s, an average degradation rate of ∼0.5 $mVcycle^{-1}\,s^{-1}$ at 1.2 Acm^{-2}_{MEA} is obtained. This is in reasonable agreement with the degradation rate of ∼0.3 $mVcycle^{-1}\,s^{-1}$ obtained for SUSDs conducted at 40 °C for cathodes with non-graphitized Vulcan carbon support reported by Mittermeier et al.[26] The mitigated MEA was also tested by the same SUSD protocol and the potential profile measured at 1.2 Acm^{-2}_{MEA} vs SUSD cycling is compared to the non-mitigated MEA in Fig. 6a (dark purple line/symbols). The potential profile of the mitigated MEA at 1.2 Acm^{-2} is clearly distinct from that of the non-mitigated MEA, as it shows a much larger potential loss in the initial 100 SUSD cycles. This initially rapid degradation is followed by a more gradual voltage decay, so that between 200 and 500 SUSD cycles the residence time normalized degradation rate for the mitigated and the non-mitigated MEA become essentially identical (∼0.4 $mVcycle^{-1}\,s^{-1}$). While both types of MEAs have the same initial performance (i.e., ∼0.64 V at 1.2 Acm^{-2}), owing to its initially faster SUSD degradation, the mitigated MEA has a ∼40 mV lower performance after 500 SUSD cycles compared to the non-mitigated MEA. This overall ∼40 mV larger voltage loss of the mitigated MEA is apparently due to its initial rapid performance loss and must thus be related to some additional degradation phenomenon originating from IrO_2/TiO_2 anode co-catalyst in the mitigated MEA.

To further explore this hypothesis, it is instructive to first examine the changes of the anode potential over the course of an SUSD cycle. Under the normal operating conditions of an H_2-fed PEMFC anode, the anode potential (and thus the potential of the IrO_2/TiO_2 anode co-catalyst) is at ∼0 V vs RHE. On the other hand, once the H_2 gas in the anode compartment has been replaced by air during an SUSD half-cycle, the anode potential increases to ∼1.05 V vs RHE.[28] During a subsequent SUSD half-cycle (i.e., when replacing the air in the anode again by H_2), the anode potential will be decreased again to ∼0 V vs RHE. Thus, over the course of a complete SUSD cycle, the anode potential is being moved in a square-wave like fashion from ∼0 to ∼1.05 and back to ∼0 V vs RHE. These potential cycles, repeated for each SUSD cycle, are well known to lead to the dissolution of iridium (via the formation of Ir^{n+} ions), a mechanism called transient dissolution[61,63] (the same process is also responsible for the accelerated dissolution of platinum during the current- or voltage-cycling of fuel cell cathodes).[62] The stability of iridium against transient dissolution strongly depends on its chemical and morphological nature. It has been previously shown that transient dissolution rates are ∼2 orders of magnitude higher for metallic Ir compared to highly crystalline IrO_2 (usually obtained by heat-treatment),[64] and comparable transient dissolution rates have been observed between metallic Ir surfaces and E-IrO_x (the product of electrochemical oxidation of

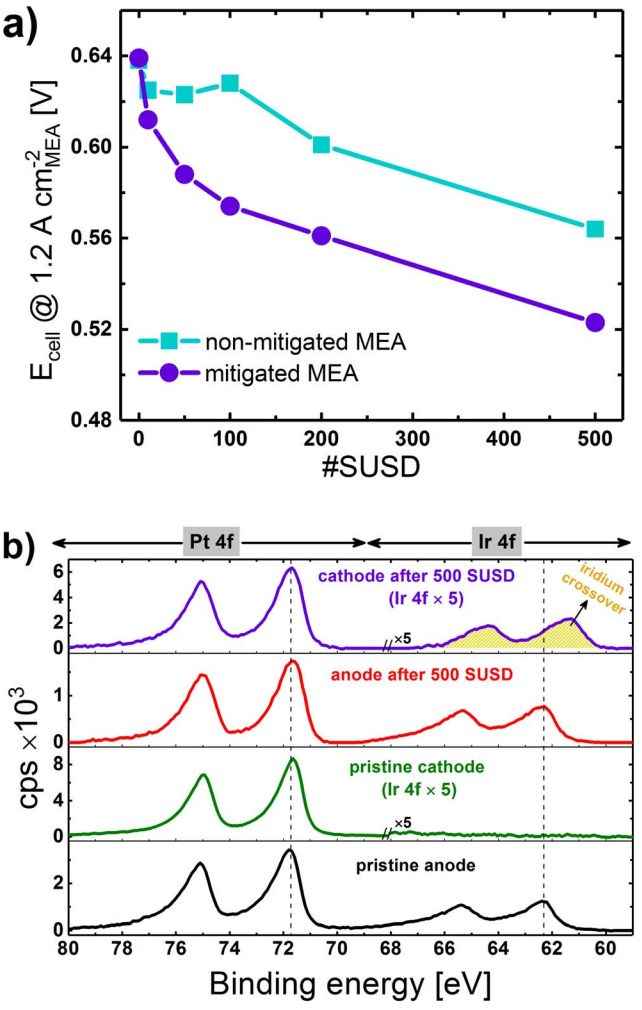

Figure 6. **(a)** Cell voltages at 1.2 Acm^{-2} (taken from H_2/air performance curves, not shown here) as a function of the performed start-up/shut-down (SUSD) cycles (acc. to the US DRIVE Fuel Cell Technical Team Roadmap protocol at 35 °C, see experimental section) for *non-mitigated* and *mitigated MEAs*. H_2/air performance curve condition: T_{cell} = 80 °C, RH = 100%, P_{cell} = 150 $kPa_{abs,outlet}$, s = $1.5_{H2}/2_{air}$. MEA specifications: i) cathode with 0.3 $mg_{Pt}cm^{-2}_{MEA}$ loading, ii) anodes with 0.05 $mg_{Pt}cm^{-2}_{MEA}$ (*non-mitigated MEA*) or with 0.05 $mg_{Pt}cm^{-2}_{MEA}$ + 0.05 $mg_{Ir}cm^{-2}_{MEA}$ (Pt/C + IrO_2/TiO_2, *mitigated MEA*) loading. (**b**) Shirley background-corrected XPS Pt 4 f and Ir 4 f spectra of the anode and cathode electrodes of the pristine and 500-SUSD cycled mitigated MEAs. The vertical dashed line in the Pt 4 f region shows the position of the Pt 4 f7/2 peaks in the spectra of all electrodes. The vertical dashed line in the Ir 4 f region shows the position of the Ir 4f7/2 peaks of the spectra of the anode electrodes (corresponding to the binding energy of A-IrO_x, see Table I). For better visualization of iridium crossover into the cathode electrode, the cps values in the Ir 4f regions of the cathode electrodes have been multiplied by 5.

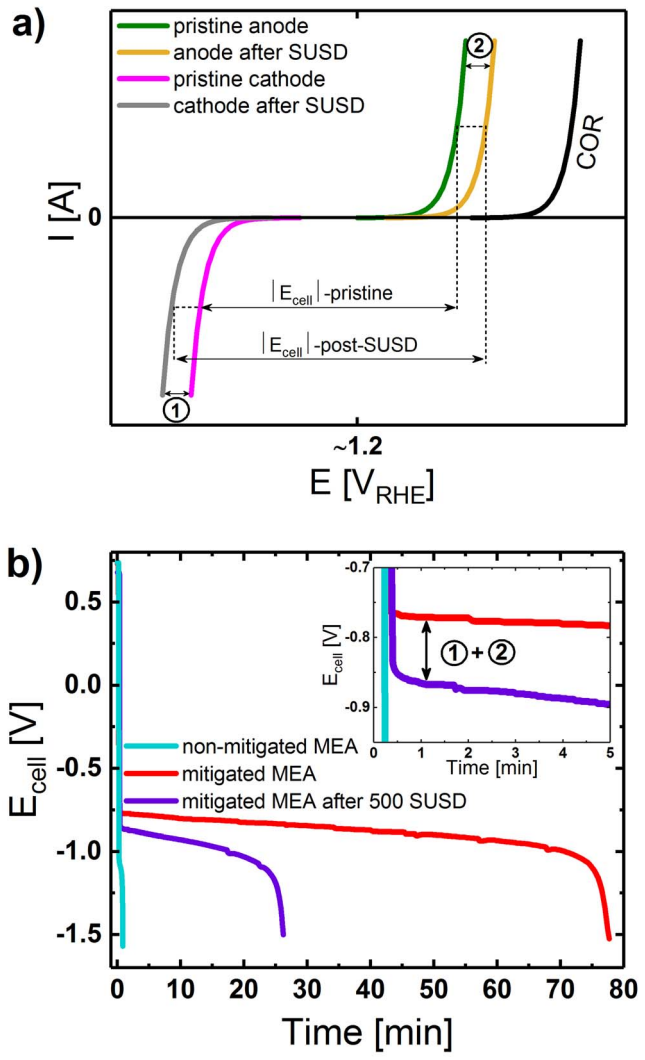

Figure 7. (**a**) Schematic representation of the current vs potential (referenced vs RHE) relationships of the anode and cathode half-cell reactions during a CRT. For the pristine mitigated MEA with an anode co-catalyst (Pt/C + IrO_2/TiO_2) and a Pt/C cathode these are: i) ORR on the pristine cathode (pink line); ii) OER on the pristine anode (green line); iii) carbon oxidation reaction (COR; black line), whose kinetics are much slower than that of the OER on an iridium based OER catalyst. For the mitigated MEA after SUSD testing, the loss of ORR performance of the cathode electrode (see Fig. 6a) leads to a negative-shift of the ORR (gray line) by a value marked as ①, while a decrease of the OER activity of the anode co-catalyst would lead to a positive-shift of the OER (yellow line) by a value marked as ②. The negative cell voltage during a CRT for a pristine mitigated MEA is marked by $|E_{cell}|$-pristine and that of the mitigated MEA after SUSD testing by $|E_{cell}|$-post-SUSD; the difference between these two cell voltages corresponds to the loss of OER and ORR performance caused by SUSD testing, i.e., to ①+②. (**b**) Cell reversal tests (CRTs) of the pristine non-mitigated MEA (turquoise line) as well as of the mitigated MEAs either in pristine state (red line) or after the 500 SUSD cycles shown in Fig. 6a (dark purple line); the MEA specifications are the same as given in Fig. 6a. CRT condition: i = 0.2 Acm^{-2}_{MEA}, $T_{cell} = 80°C$, RH = 100%, $P_{cell} = 150\ kPa_{abs,outlet}$, N_2/air flows (166/333 nccm) in anode/cathode. The inset is a magnified view of the first 5 min of the CRTs, marking the initial cell potential difference between the two mitigated MEAs, corresponding to the sum of the ORR and OER activity losses (denoted as ①+② in the inset of panel b).

metallic Ir by potential cycling between ~0–1.05 V vs RHE)[61,63] rendering metallic Ir and E-IrO_x substantially less stable than heat-treated IrO_2 when subjected to voltage cycles. Considering that the here used IrO_2/TiO_2 catalyst was heat-treated above 300 °C according to the patent[65] and that its voltammetric features are indicative of highly crystalline IrO_2 (see black line in Fig. 5b), one would expect it to have a high stability against transient dissolution during SUSD cycling. However, according to the data shown in Fig. 5d, the near-surface layers of the IrO_2/TiO_2 anode co-catalyst can be reduced to metallic iridium (from the surface to the core of the catalyst particles, see Fig. 5c) within a few hours when exposed to the H_2 environment of a PEMFC anode at ~0 V vs RHE during the conditioning and recording of a polarization curve (see experimental section). This, combined with the fact that metallic iridium surfaces (and their electrochemical oxidation product, E-IrO_x) exhibit very high transient dissolution rates, render it very likely that there might be substantial iridium dissolution from the anode co-catalyst during SUSD cycles; if true, this could lead to an iridium loss from the anode electrode and to iridium re-precipitation in the membrane or in the cathode electrode.

In order to examine whether iridium dissolution during SUSD cycles leads to a diffusion and re-precipitation of iridium in the oxygen (cathode) electrode, the mitigated MEA was harvested after 500 SUSD cycles and examined by XPS. Figure 6b shows the XPS Pt 4 f and Ir 4 f spectra of the pristine and SUSD cycled anode and cathode electrodes of the mitigated MEA. All the spectra exhibit Pt 4 f doublets with Pt 4f7/2 peaks at ~71.8 eV (vertical dashed line in Pt 4 f region), indicating that the surface chemistry of the platinum catalyst in both anode and cathode does not change over the 500 SUSD cycles. The Ir 4 f spectra of the pristine and the SUSD cycled anodes are very similar to those of the as-received IrO_2/TiO_2 catalyst powder (bottom panel in Fig. 4a), with Ir 4f7/2 peaks at ~62.2 and ~62.1 eV, respectively. Based on the analysis presented in Table I, the Ir 4 f spectra of the as-received IrO_2/TiO_2 catalyst are composed of signals from amorphous (A-IrO_x) and crystalline (C-IrO_2) iridium oxide. Although it is expected that the near-surface layers of the IrO_2/TiO_2 anode co-catalyst will be partially reduced to metallic Ir during the initial conditioning step and recording of a polarization curve, a metallic Ir signal (~60.9 eV, see Table I) is not detected in the SUSD cycled anode spectrum. This is most likely due to the electrochemical oxidation of metallic Ir and transition to E-IrO_x by potential cycling between ~0–1.05 V vs RHE during SUSD cycles, where it is reported that E-IrO_x is composed of two different iridium oxide species with Ir4f binding energies comparable to the as-received IrO_2/TiO_2 catalyst in this study.[66] Therefore, the Ir4f signal in the SUSD cycled anode spectrum should predominantly reflect the contribution of E-IrO_x as well as the contribution from the sub-surface IrO_2 of the IrO_2/TiO_2 catalyst that did not get reduced to metallic Ir during the experiments. Note that a significant fraction of sub-surface IrO_2 was also observed in the XPS spectrum of the TGA-1h-120 °C sample in Fig. 4a, even though ~50% of the IrO_2 in this sample was reduced to metallic near-surface Ir during the TGA experiment (see blue line in Fig. 3a).

With regards to the XPS spectra of the cathode electrodes, no Ir 4 f signal is detected for the pristine cathode, as it only contains the Pt/C catalyst. However, a relatively strong Ir 4 f signal could be detected in the XPS spectrum of the cathode electrode after 500 SUSD cycles, indicating iridium dissolution in the anode electrode and subsequent permeation of Ir^{n+} species through the membrane to the cathode electrode (often referred to as crossover). The Ir 4f7/2 peak energy of ~61.2 eV observed for the SUSD cycled cathode is between the characteristic binding energy of metallic iridium (~60.9 eV, see Table I) and that observed for E-IrO_x (~61.6 eV for Ir(IV) contribution in E-IrO_x) in our previous study.[66] The cathode electrode experiences a potential cycling between ~0.95 to >1.4 V vs RHE during SUSD cycles (more details about potential profile of the cathode electrode during SUSD cycles are provided in the last section). This consequently promotes the oxidation of iridium in cathode during the course of SUSD experiment.[61] On the other hand, during the measurement of H_2/air polarization curves at different SUSD cycling intervals, the cathode electrode potential

remains at values below 0.65 V vs RHE for the course of several minutes during each polarization curve, a potential region in which metallic Ir is thermodynamically stable.[67] Therefore, the nature of such iridium surface contaminations in the SUSD cycled cathode electrode could be essentially prone to the potential profile experienced by the cathode electrode during the experiments. Hence, the identification of the exact nature of iridium in the SUSD cycled cathode electrode is not trivial. However, the ORR activity loss of the mitigated MEA within the first ∼100 SUSD cycles that was observed in Fig. 6a could be explained by assuming that iridium dissolved in the anode is deposited on the platinum surface of the Pt/C cathode catalyst; owing to the ∼100-fold lower ORR activity of iridium compared to platinum, this would lead to a loss of ORR activity of the Pt/C cathode catalyst.[68–70] This phenomenon would be analogous to the observations made in the context of (partial) Ru dissolution from PtRu alloy anode catalysts in direct methanol fuel cells or in PEMFCs operated with reformate, where the dissolved Ru species were shown to permeate through the membrane to the cathode and to deteriorate the ORR performance of the Pt/C cathode catalyst.[71–74] Based on these considerations, the overall ∼40 mV higher potential loss over 500 SUSD cycles for the mitigated MEA (Fig. 6a) can be assigned to the poisoning of the ORR activity of the Pt/C cathode catalyst by re-deposited crossover iridium. It should be noted that iridium dissolution was also observed when using the same IrO_2/TiO_2 catalyst as oxygen evolution catalyst in a PEM water electrolyzer that was cycled between OCV and electrolysis mode.[29] During the OCV periods, the oxygen electrode (anode) potential dropped to ∼0 V vs RHE due to H_2 permeation through the membrane into the anode compartment, while during operation, the anode potential was above 1.5 V vs RHE. In this case, however, the dissolved iridium was precipitated in the H_2-saturated membrane phase, which prevented iridium crossover to the hydrogen electrode (cathode).

Cell reversal for pristine or SUSD cycled MEAs.—Cell reversal tests (CRTs) were performed on pristine and SUSD cycled mitigated MEAs (Pt/C + IrO_2/TiO_2 anode) to determine the effect of the SUSD induced iridium dissolution on the CRT tolerance of mitigated MEAs; as a reference, a CRT was also performed for the pristine non-mitigated MEA (Pt/C anode). In order to initiate the CRT, the anode gas was switched from H_2 to N_2, while air was continuously fed to the cathode electrode and a current density of 0.2 $Acm^{-2}{}_{MEA}$ was applied. Upon the replacement of H_2 by N_2, the anodic current initially supplied by the hydrogen oxidation reaction (HOR) will have to be provided by a combination of the oxygen evolution reaction (OER; see green line in Fig. 7a) and the carbon oxidation reaction acc. to Eq. 1 (COR; see black line in Fig. 7a), whose relative contribution to the overall current depends on the OER activity of the anode catalyst(s) and on the nature of the carbon support materials (graphitized carbon supports being more stable than non-graphitized ones).[75] The higher the OER/COR activity ratio at a given potential and at a given overall current density, the lower will be the degradation of the anode carbon support over the course of a CRT, i.e., the higher will be the CRT tolerance of an MEA. As the OER and COR currents are only appreciable above ∼1.3–1.4 V vs RHE and as the cathode potential in a PEMFC ranges between ∼0.7–0.9 V vs RHE (see pink line in Fig. 7a), the cell voltage during cell reversal becomes negative ($E_{cell} \equiv E_{cathode}—E_{anode}$) and is marked by the horizontal arrows in Fig. 7a. As the anode electrode degrades over the course of a CRT (predominantly due to anode carbon support corrosion), the cell voltage becomes more and more negative; in this work, the time to reach a cell voltage of −1.5 V was set as the end-of-life (EOL) criterion and is further on referred to as *reversal tolerance time* of the MEAs.

Figure 7b shows the CRT for the non-mitigated MEA (turquoise line) as a reference, with a reversal tolerance time of only ∼36 s. This very rapid degradation is due to the poor OER activity of a Pt/C catalyst, so that its OER kinetics are similar or even slower than the COR of the graphitized carbon support.[4,19,75] In the context of the scheme in Fig. 7a, this means that the green line marking the OER kinetics would be shifted positively and would be located at or to the right of the black line marking the COR. In this case, the overall current will be carried to a comparable fraction by both the OER and the COR, leading to a rapid corrosion of the carbon support, which in turn leads to the collapse of the anode catalyst layer and to cell failure.

In contrast to the non-mitigated MEA, the use of IrO_2/TiO_2 as an anode co-catalyst in the mitigated MEA drastically increases the reversal tolerance time to ∼77 min. This is due to the much higher OER activity of IrO_2/TiO_2 compared to Pt/C, illustrated in Fig. 7a by the green line for the OER, resulting in a lower anode potential and, consequently, a much lower fraction of the overall current contributed by the COR. Here it should be noted that the OER activity of the IrO_2/TiO_2 catalyst when used as anode co-catalyst is even higher than the OER activity of the as-received material, due to the enhanced OER activity of the (partially) reduced IrO_2 phase compared to the initially crystalline IrO_2 (compare yellow and black lines in Fig. 5e) that is formed within hours under the conditions of a H_2 anode (see Fig. 5d). As a corollary, a non-reducible IrO_2 based catalyst would exhibit a lower reversal tolerance due to its lower OER activity. While the SUSD cycling induced iridium dissolution in the anode of the mitigated MEA leads to an ORR activity loss of ∼120 mV at 1.2 Acm^{-2} (see dark purple line/symbols in Fig. 6a) and of ∼35 mV at 0.2 Acm^{-2} (data not shown), this would not affect the cell reversal tolerance of the mitigated MEA, as this would not affect the anode potential during cell reversal (green line in Fig. 7a) and thus would not affect the rate of the COR, even though the cell voltage during the CRT would be more negative. Therefore, in this case, one would expect identical cell reversal tolerance for the pristine and for the SUSD cycled mitigated MEA. The cell reversal tolerance would only be affected negatively, if i) the OER activity of the IrO_2/TiO_2 anode co-catalyst would decrease over the course of SUSD cycling (illustrated by the yellow line in Fig. 7a), and/or if ii) the anode carbon support would be partially corroded by the SUSD cycling due to the H_2/air front induced anode potential cycles (see above). The latter is highly unlikely, as only minor anode thinning (∼10%), indicating little carbon support corrosion was observed after 500 SUSD/voltage cycles at 80 °C for a non-graphitized Vulcan carbon support,[28] so that for the here conducted 500 SUSD cycles at 35 °C and graphitized Vulcan carbon support, anode carbon support corrosion can be considered negligible (anode thinning of ≪10%) due to the high apparent activation energy of the COR.[75] Whether the SUSD induced iridium dissolution will also affect the OER activity, and thus the cell reversal tolerance of the mitigated MEAs, will be examined in the following.

As shown in Fig. 7b, the cell reversal tolerance time of the mitigated MEA that was subjected to the 500 SUSD cycles (see Fig. 6a) prior to the CRT is ∼3-fold shorter (∼26 min; see dark purple line in Fig. 7b) than that of the pristine mitigated MEA. In addition, as shown in the inset of Fig. 7b, the initial CRT cell voltage of the SUSD cycled mitigated MEA (dark purple line) is ∼88 mV lower compared to the pristine mitigated MEA (red line). Since the cell voltage during a CRT is the difference between the cathode (ORR) and the anode (OER) half-cell potentials, as shown schematically in Fig. 7a, the lower cell voltage of the SUSD cycled mitigated MEA (denoted as ①+② in the inset of Fig. 7a) must originate from a half-cell potential shift of either the ORR (marked by ① in Fig. 7a) and/or the OER (marked by ②). Here it should be noted that with an anode carbon loading of 0.2 $mgcm^{-2}{}_{MEA}$ in this study, if all of the carbon support were to corrode at the end of CRT in the anode electrode through Eq. 1 ($4e^-/CO_2$), it would correspond to a maximum COR charge of ∼6.4 C $cm^{-2}{}_{MEA}$. The overall charge that is drawn at the end of CRT is ∼924 C $cm^{-2}{}_{MEA}$ and ∼312 C $cm^{-2}{}_{MEA}$ for the mitigated MEA (red curve in Fig. 7b) and mitigated MEA after 500 SUSD cycles (dark purple curve in

Fig. 7b), respectively. This would signify that the maximum time averaged COR contribution to the overall drawn charge (OER + COR) during CRT would only be ~0.7% and ~2.1% for the mitigated MEA (red curve in Fig. 7b) and mitigated MEA after 500 SUSD cycles (dark purple curve in Fig. 7b), respectively. Hence, the contribution of the COR to the overall anodic current can be neglected when using a highly active OER anode co-catalyst. Based on the H_2/air performance curves recorded over the course of the SUSD test (data not shown), the increase of the ORR overpotential at 0.2 Acm^{-2} after 500 SUSD cycles is ~35 mV (≡ ①). Thus, the difference between this value and the ~88 mV lower initial CRT voltage, equating to ~53 mV, can only be ascribed to a loss in OER activity of the IrO_2/TiO_2 anode co-catalyst after the 500 SUSD cycles, thereby corresponding to a positive-shift of the OER potential as compared to the pristine mitigated MEA at the beginning of CRT (≡ ②). Such loss in OER activity would increase the anode potential and would thus increase the fractional CRT current that is provided by the COR, leading to the observed decrease of the reversal tolerance time.

There are two possible hypotheses to explain the loss of OER activity of the IrO_2/TiO_2 anode co-catalyst that is apparently induced by SUSD cycling: i) dissolution of iridium from the anode catalyst during SUSD transients, leading to an overall loss of OER active material in the anode; and/or, ii) dissolution of Pt from the Pt/C anode catalyst due to anode voltage cycling during the SUSD transients and re-deposition of the dissolved Pt^{n+} species on the $Ir/IrO_2/TiO_2$ anode co-catalyst, lowering its OER activity by blocking the OER active iridium surface sites. The former would require a substantial loss of iridium from the anode: at a Tafel slope for the OER of ~50–60 mV $decade^{-1}$,[31] a loss of 90% of the active iridium sites would lead to an OER activity loss of ~50–60 mV. Considering a ~7.5 nm thick layer of IrO_2 covering the TiO_2 support in the IrO_2/TiO_2 catalyst (see Fig. A·1, inset), the dissolution of iridium from the surface of the catalyst would constantly expose the underlying iridium active sites in the IrO_2 layer, which would consequently participate into OER; therefore, no apparent loss of OER activity is expected until the last few mono-layers of IrO_2 covering the TiO_2 support particles start to dissolve. As the ratio between the Pt 4 f and the Ir 4 f XPS spectra of the pristine and the SUSD cycled anodes in Fig. 6b do not indicate such high losses of iridium after 500 SUSD cycles, a poisoning of OER active iridium sites by re-deposited platinum seems more likely.

Summary of the SUSD induced processes and their effect on the CRT tolerance.—In order to summarize the foregoing analysis and discussion, a schematic representation of the processes occurring in the mitigated MEA with an IrO_2/TiO_2 anode co-catalyst during the normal operation of a PEMFC and during the shut-down and the start-up half-cycles of an SUSD test are shown in Fig. 8. When using an IrO_2 based anode co-catalyst for mitigating cell reversal damages in PEMFCs, it was shown above that the near-surface layer(s) of the IrO_2/TiO_2 catalyst get chemically reduced to metallic Ir by H_2 during the normal operation of the fuel cell, as illustrated in Fig. 8a. Such chemical alteration of the catalyst surface should improve its reversal tolerance time in a CRT, since metallic iridium that converts to electrochemically oxidized (often referred to as E-IrO_x) or hydrous iridium oxide once the potential is increased into the OER region has a higher intrinsic OER activity than the initial heat-treated, highly crystalline IrO_2.

At the same time, however, metallic Ir is reported to exhibit a ~2 orders of magnitude higher dissolution rate than crystalline IrO_2,[64] rendering it more prone to dissolution during the SUSD induced anode potential cycles (~0–1.05 V vs RHE).[28] During the fuel cell shut-down step, described in Fig. 8b, the passage of the air-front pushes the H_2 from anode inlet to the anode outlet (from bottom to top in Fig. 8b), whereby the anode potential increases from ~0 V vs RHE (in the H_2-filled segment) to ~1.05 V vs RHE (in the air-filled segment). This leads to platinum and iridium dissolution from the anode catalysts, forming Pt^{n+} and Ir^{n+} ions that are dissolved in the ionomer phase and can diffuse across the anode, the membrane, and the cathode. As the air-front passes through the anode, the cathode segment adjacent to the air-filled anode will be at potentials of >1.4 V vs RHE. After the passage of the air-front, the cathode potential will also assume ~1.05 V vs RHE[8] (the cell voltage being ~0 V); whether re-deposition of Pt^{n+} and Ir^{n+} (possibly also in form of underpotential deposition on Pt) will occur at such high potential on the Pt/C cathode catalyst is still an open question. In the subsequent start-up step, described in Fig. 8c, a H_2-front passes from the anode inlet to the anode outlet, displacing air from the anode compartment. In the H_2-filled anode segment, the potential drops to ~0 V vs RHE and the dissolved Pt^{n+} and Ir^{n+} species will deposit on the surface of the anode catalysts. As the nucleation of metallic Pt and Ir is expected to be more facile on metal surfaces compared to nucleation of nanoparticles on the carbon support, one would expect that the dissolved metals deposit preferentially on the platinum and iridium phases. Since the HOR activity of iridium is very high and only ~3-fold lower than the that of platinum,[36] this would not affect the HOR performance of the anode. On the other hand, since the OER activity of iridium based catalysts is orders of magnitude higher than that of platinum,[76] a deposition of platinum

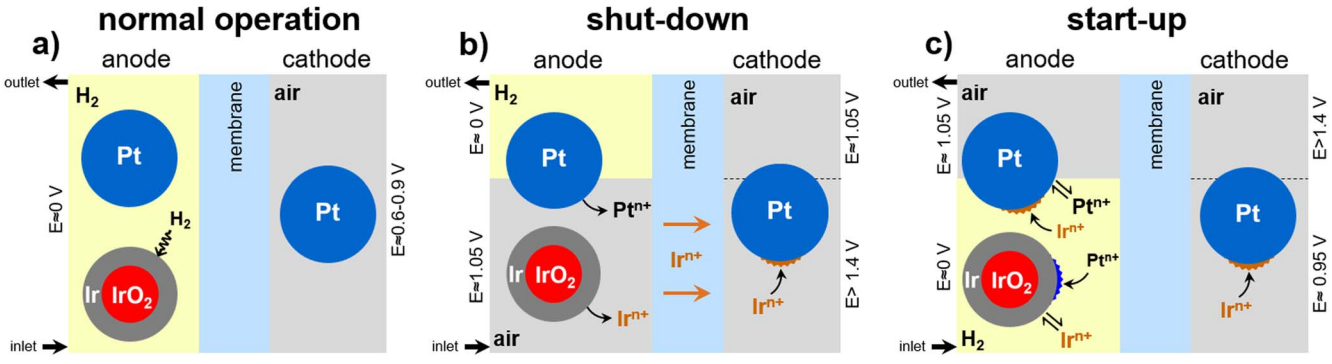

Figure 8. Schematic representation of the processes occurring in a mitigated MEA in the presence with an iridium oxide based anode co-catalyst during normal fuel cell operation, fuel cell shut-down, and fuel cell start-up. (**a**) *Normal fuel cell operation:* illustrating the chemical reduction of the near-surface layer(s) of the iridium oxide phase of the IrO_2/TiO_2 anode co-catalyst by H_2 to metallic Ir. (**b**) *Fuel cell shut-down step:* upon passage of the air-front, the anode potential increases to ~1.05 V vs RHE,[28] leading to platinum and iridium dissolution from the anode catalysts, whereby the resulting Pt^{n+} and Ir^{n+} ions can diffuse within in the ionomer and membrane phase; after passage of the air-front, the cathode potential will assume ~1.05 V,[8] and re-deposition of crossover iridium on the platinum surface of the Pt/C cathode catalyst could possibly occur. (**c**) *Fuel cell shut-down step:* upon passage of the H_2-front, the anode potential decreases from ~1.05 V to ~0 V vs RHE, and the re-deposition of Pt^{n+} and Ir^{n+} on the Pt/C and the IrO_2/TiO_2 catalysts in the anode will occur; after passage of the H_2-front, the cathode potential is ~0.95 V (this lower OCV is due to H_2 crossover), and iridium deposition on the Pt/C cathode catalyst becomes more likely.

on the surface of the IrO_2/TiO_2 anode co-catalyst would be expected to drastically reduce its OER activity. Once the H_2-front has passed, the open circuit potential of the cathode electrode will be lowered to ~0.90–0.95 V vs RHE due to the H_2 permeation through membrane (corresponding to the OCV of a H_2/air cell), at which potential the (underpotential) deposition of iridium ions dissolved in the ionomer phase of the cathode electrode (as well as the deposition of dissolved platinum ions) on the Pt/C cathode catalyst will likely occur. As iridium has a much lower ORR activity than Pt,[68–70] (underpotential) deposition of iridium on the platinum of the cathode catalyst would lead to the lower ORR activity after SUDS cycles, as deduced from Fig. 6a. In summary, our analysis suggests that the ~3-fold lower reversal tolerance time observed for the mitigated MEA after 500 SUSD cycles is most likely due to a loss of OER activity of the anode co-catalyst caused by the transient dissolution of platinum from the anode Pt/C catalyst and its partial deposition on the surface of the iridium phase of the IrO_2/TiO_2 anode co-catalyst. It has to be mentioned that during the start-up process, any dissolved Pt or Ir will immediately re-deposit on the parent particle due to the low anode potential in the presence of H_2 (a similar phenomenon was suggested for Pt by Schwämmlein et al.[28]), so that Ir^{n+} crossover to the cathode can be neglected during the start-up process and should be mainly occurring during the shut-down process. Based on the here proposed mechanisms, the degradation of the ORR activity of the Pt/C cathode catalyst during SUSD cycles could be avoided, if the chemical reduction of the active iridium oxide phase of the IrO_2/TiO_2 anode co-catalyst could be prevented. Thus, future research towards the development of a more stable anode co-catalyst to mitigate cell reversal degradation would be to focus on stabilization strategies to hinder the chemical reduction of iridium oxide based catalysts by H_2 at the operational temperatures of PEMFCs, along with designing high OER active IrO_2 catalysts. However, whether Pt would deposit on the surface of a non-reducible iridium oxide based anode co-catalyst and equally degrade its OER activity upon SUSD cycling is still an open question, which requires further investigation in future studies.

Conclusions

In this study, it is shown that when using an IrO_2 based anode co-catalyst for mitigating cell reversal damages in PEMFCs, the near-surface layer(s) of the IrO_2/TiO_2 catalyst get chemically reduced to metallic Ir by H_2 during the normal operation of the fuel cell. Such alteration of the near-surface layer(s) of IrO_2 drastically affects its stability during the anode potential transients during SUSD cycles, where it was shown that the dissolution of metallic Ir and crossover of the dissolved Ir^{n+} species through the membrane to the cathode electrode cause iridium deposition on the Pt/C cathode catalyst, as evidenced by XPS Ir4f spectra of the cathode electrodes after SUSD cycling. Such iridium-based contamination on the cathode catalyst surface deteriorates the ORR activity of Pt and results in a significant performance loss during the normal operation of the fuel cell. At the same time, SUSD transients also cause an OER activity loss of the anode co-catalyst, which was shown to be mainly due to the re-deposition of Pt dissolved from the anode HOR catalyst onto the reduced IrO_2 anode co-catalyst, blocking its OER active sites.

In light of the here made observations, it is clear that the reduction of the near-surface layer(s) of the IrO_2 anode co-catalyst to metallic Ir compromises its stability during the anode potential transients that occur during SUSD cycles. Therefore, it is suggested that the stability of IrO_2-based anode co-catalysts in H_2-containing atmosphere should be carefully evaluated by a here proposed new methodology prior to using the catalysts in a PEMFC anode. It is based on an extended isothermal TGA experiment at operational temperatures of PEMFCs and under a dilute H_2 atmosphere, where the reducibility of the IrO_2 catalyst can be reliably and quantitatively examined. After the isothermal TGA experiment, the catalyst powder can be electrochemically investigated by RDE experiments in order to determine the effect of the exposure of the catalyst to a reducing H_2 atmosphere on its electrochemical properties.

Last but not least, future research towards the development of new anode co-catalysts should focus on stabilization strategies to hinder the chemical reduction of iridium oxide based catalysts by H_2 at the operational temperatures of PEMFCs, along with designing highly OER active IrO_2 catalysts.

Acknowledgments

The authors gratefully acknowledge the German Ministry of Education and Research for financial support of this work within the innoKA project (BMWi, 03ET6096A). The authors would also like to thank Anna T.S. Freiberg, Philipp J. Rheinländer, and Julien Durst for fruitful scientific discussions (Chair of Technical Electrochemistry, Technical University of Munich, Germany). Thanks are also extended to Burak Koyuturk and Paulette A. Loichet Torres (Chair of Technical Electrochemistry, Technical University of Munich, Germany) for their help during the XPS measurements.

Appendix

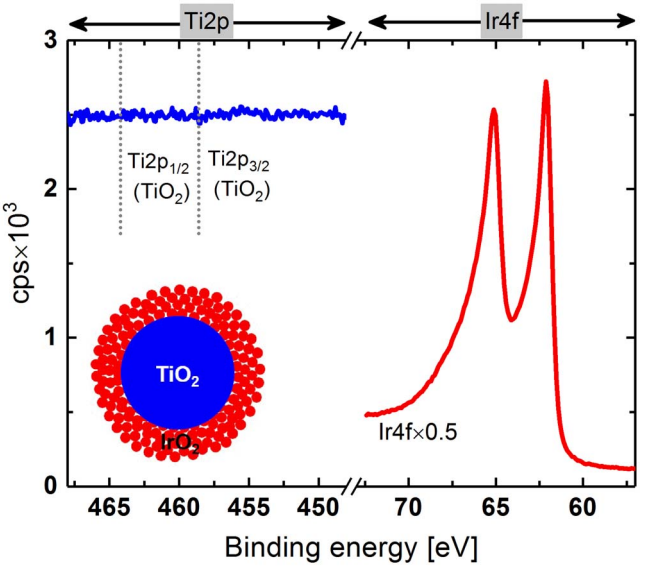

Figure A·1. XPS Ti2p and Ir4f spectra of as-received IrO_2/TiO_2 catalyst. The vertically dashed lines in Ti2p region represent the positions of $Ti2p_{3/2}$ and $Ti2p_{1/2}$ signals in a TiO_2 sample.[77] The Ir4f signal is multiplied by 0.5 for a better representation of the data. Inset shows schematic representation of a TiO_2 support particle, which is completely covered by IrO_2 particles. If the IrO_2 layer is assumed as a uniform and compact film covering the TiO_2 support particle ($d_{TiO2} \approx 28$ nm), an equivalent IrO_2 film thickness of ~7.5 nm can be consequently calculated for this structure.

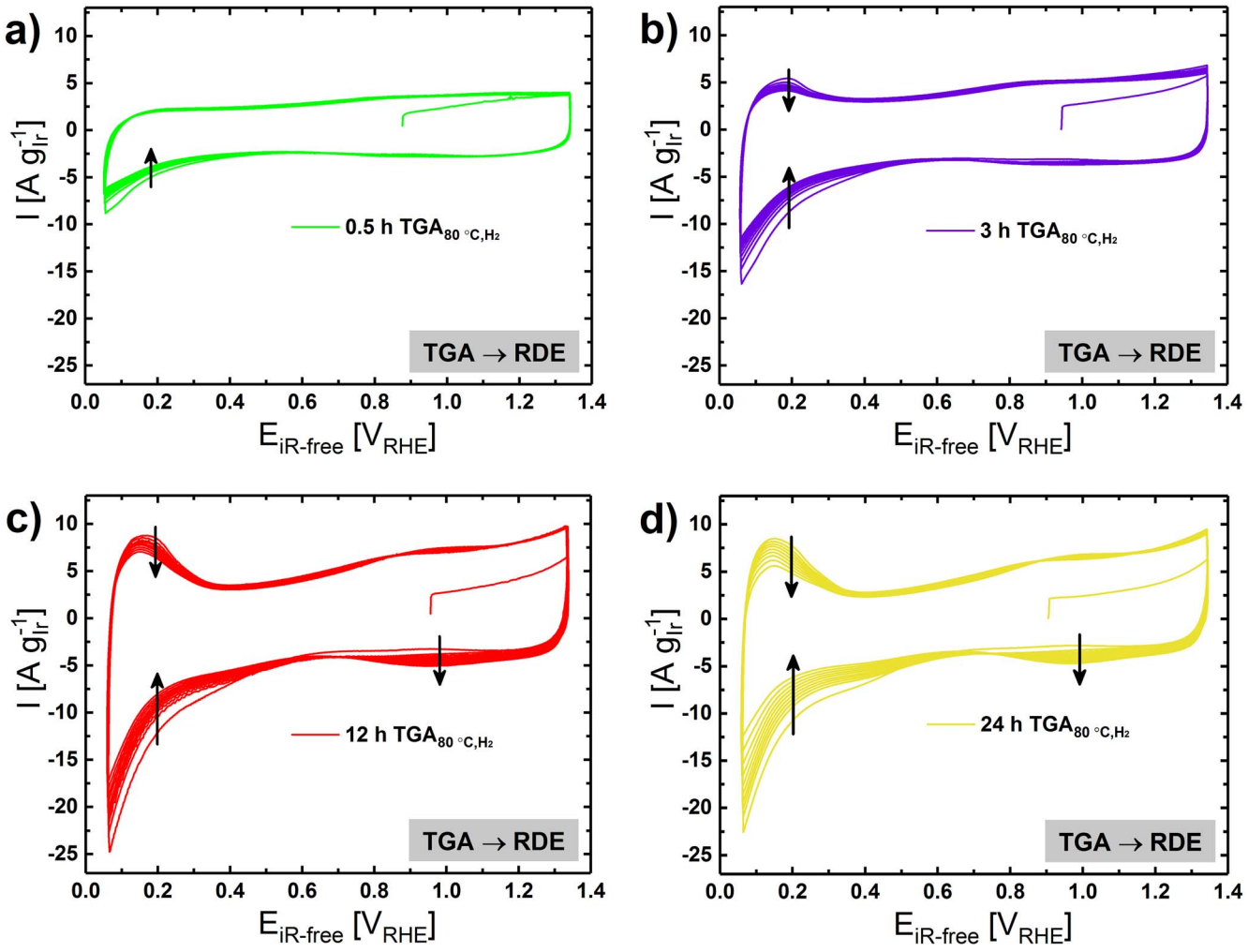

Figure A·2. The initial 10 cyclic voltammograms (CVs) of the partially reduced IrO_2/TiO_2 samples marked in Fig. 5a, namely after (**a**) 0.5 h, (**b**) 3 h, (**c**) 12 h, and (**d**) 24 h of the TGA isothermal experiment at 80 °C. In order to plot Fig. 5b, the first voltammetric cycles out of the measured 10 cycles were taken, whereby the initial anodic going sweeps from OCP (~0.9 V_{RHE}) to 1.35 V_{RHE} were removed. The arrows show the evolution of the CVs from cycle 1 to 10. The RDE measurements conditions are the same as given in Fig. 5b.

ORCID

Mohammad Fathi Tovini https://orcid.org/0000-0003-4334-4471
Hubert A. Gasteiger https://orcid.org/0000-0001-8199-8703

References

1. (https://energy.gov/eere/vehicles/downloads/us-drive-fuel-cell-technical-team-roadmap) (accessed on 03.02.2021) USDRIVE, *Fuel Cell Technical Team Roadmap*.
2. Y. Wang et al., *Int. J. Hydrogen Energy*, **45**, 996 (2020).
3. P. Mandal, B. K. Hong, J.-G. Oh, and S. Litster, *J. Power Sources*, **397**, 397 (2018).
4. B. K. Hong, P. Mandal, J.-G. Oh, and S. Litster, *J. Power Sources*, **328**, 280 (2016).
5. T. R. Ralph, S. Hudson, and D. P. Wilkinson, *ECS Trans.*, **1**, 67 (2006).
6. J. P. Meyers and R. M. Darling, *J. Electrochem. Soc.*, **153**, A1432 (2006).
7. R. L. Borup, D. D. Papadias, R. Mukundan, D. Spernjak, D. A. Langlois, R. Ahluwalia, K. L. More, and S. Grot, *ECS Trans.*, **69**, 1029 (2015).
8. R. Makharia, S. Kocha, P. Yu, M. A. Sweikart, W. Gu, F. Wagner, and H. A. Gasteiger, *ECS Trans.*, **1**, 3 (2006).
9. I. C. Halalay, S. Swathirajan, B. Merzougui, M. P. Balogh, G. C. Garabedian, and M. K. Carpenter, *J. Electrochem. Soc.*, **158**, B313 (2011).
10. C. Gebauer, Z. Jusys, and R. J. Behm, *J. Electrochem. Soc.*, **165**, J3342 (2018).
11. J. Wu, X. Z. Yuan, J. J. Martin, H. Wang, J. Zhang, J. Shen, S. Wu, and W. Merida, *J. Power Sources*, **184**, 104 (2008).
12. M. L. Perry, T. Patterson, and C. Reiser, *ECS Trans.*, **3**, 783 (2006).
13. S. W. Lee, B. H. Lee, T.-Y. Kim, C. Baik, M. S. Kim, G. S. Chai, and C. Pak, *Catal. Commun.*, **130**, 105758 (2019).
14. C. E. Moore, F. Afsahi, A. P. Young, and E. L. Gyenge, *The Journal of Physical Chemistry C*, **123**, 23361 (2019).
15. H. Schmies et al., *Adv. Energy Mater.*, **8**, 1701663 (2018).
16. E. Hornberger et al., *ACS Catal.*, **8**, 9675 (2018).
17. J. Zhang, F. Coms, and S. Kumaraguru, *J. Electrochem. Soc.*, **168**, 024520 (2021).
18. I. Jang, I. Hwang, and Y. Tak, *Electrochim. Acta*, **90**, 148 (2013).
19. C.-W. Roh, H.-E. Kim, J. Choi, J. Lim, and H. Lee, *J. Power Sources*, **443**, 227270 (2019).
20. C. E. Moore, J. Eastcott, M. Cimenti, N. Kremliakova, and E. L. Gyenge, *J. Power Sources*, **417**, 53 (2019).
21. T. Labi, F. Van Schalkwyk, S. M. Andersen, P. Morgen, S. C. Ray, and J. Chamier, *J. Power Sources*, **490**, 229568 (2021).
22. C. Cai, Z. Wan, Y. Rao, W. Chen, J. Zhou, J. Tan, and M. Pan, *J. Power Sources*, **455**, 227952 (2020).
23. R. Marić, C. Gebauer, M. Nesselberger, F. Hasché, and P. Strasser, *J. Electrochem. Soc.*, **167**, 124520 (2020).
24. P. J. Rheinländer and J. Durst, *J. Electrochem. Soc.*, **168**, 024511 (2021).
25. C. A. Reiser, L. Bregoli, T. W. Patterson, J. S. Yi, J. D. Yang, M. L. Perry, and T. D. Jarvi, *Electrochem. Solid-State Lett.*, **8**, A273 (2005).
26. T. Mittermeier, A. Weiß, F. Hasché, G. Hübner, and H. A. Gasteiger, *J. Electrochem. Soc.*, **164**, F127 (2017).
27. T. Mittermeier, A. Weiß, F. Hasché, and H. A. Gasteiger, *J. Electrochem. Soc.*, **165**, F1349 (2018).
28. J. N. Schwämmlein, P. J. Rheinländer, Y. Chen, K. T. Freyer, and H. A. Gasteiger, *J. Electrochem. Soc.*, **165**, F1312 (2018).
29. A. Weiß, A. Siebel, M. Bernt, T. H. Shen, V. Tileli, and H. A. Gasteiger, *J. Electrochem. Soc.*, **166**, F487 (2019).
30. B. Klose-Schubert, D. Herein, and H.-G. Reitz, *EU Patent EP*, 2 608 297 A1 (2013), Awarded June 26.
31. M. Bernt, A. Siebel, and H. A. Gasteiger, *J. Electrochem. Soc.*, **165**, F305 (2018).
32. M. Bernt and H. A. Gasteiger, *J. Electrochem. Soc.*, **163**, F3179 (2016).
33. R. D. Shannon, *Acta Crystallogr., Sect. A*, **32**, 751 (1976).
34. T. Mittermeier, A. Weiß, H. A. Gasteiger, and F. Hasché, *J. Electrochem. Soc.*, **164**, F1081 (2017).
35. C. Simon, F. Hasche, D. Muller, and H. A. Gasteiger, *ECS Trans.*, **69**, 1293 (2015).

36. J. Durst, C. Simon, F. Hasché, and H. A. Gasteiger, *J. Electrochem. Soc.*, **162**, F190 (2015).
37. J. H. Flynn and L. A. Wall, *Journal of Polymer Science Part B: Polymer Letters*, **4**, 323 (1966).
38. T. Reier, M. Oezaslan, and P. Strasser, *ACS Catal.*, **2**, 1765 (2012).
39. S. J. Freakley, J. Ruiz-Esquius, and D. J. Morgan, *Surf. Interface Anal.*, **49**, 794 (2017).
40. V. Pfeifer et al., *Surf. Interface Anal.*, **48**, 261 (2016).
41. D. Yu, M. Zhu, T. A. Utigard, and M. Barati, *Miner. Eng.*, **54**, 32 (2013).
42. K. V. Manukyan, A. G. Avetisyan, C. E. Shuck, H. A. Chatilyan, S. Rouvimov, S. L. Kharatyan, and A. S. Mukasyan, *The Journal of Physical Chemistry C*, **119**, 16131 (2015).
43. J. Dang, G.-H. Zhang, and K.-C. Chou, *Int. J. Refract. Met. Hard Mater*, **41**, 356 (2013).
44. S. Watanabe, X. Ma, and C. Song, *The Journal of Physical Chemistry C*, **113**, 14249 (2009).
45. J. Li, G. Lu, G. Wu, D. Mao, Y. Guo, Y. Wang, and Y. Guo, *Catalysis Science & Technology*, **4**, 1268 (2014).
46. H. Zhu, Z. Qin, W. Shan, W. Shen, and J. Wang, *J. Catal.*, **225**, 267 (2004).
47. Z. Chen, J. Dang, X. Hu, and H. Yan, *Metals*, **8**, 751 (2018).
48. M. Venkatesh, P. Ravi, and S. P. Tewari, *The Journal of Physical Chemistry A*, **117**, 10162 (2013).
49. C. Massué, V. Pfeifer, X. Huang, J. Noack, A. Tarasov, S. Cap, and R. Schlögl, *ChemSusChem*, **10**, 1943 (2017).
50. J. Dang, K.-C. Chou, X.-J. Hu, and G.-H. Zhang, *Steel Res. Int.*, **84**, 526 (2013).
51. S. Geiger, O. Kasian, B. R. Shrestha, A. M. Mingers, K. J. J. Mayrhofer, and S. Cherevko, *J. Electrochem. Soc.*, **163**, F3132 (2016).
52. J. Mozota and B. E. Conway, *Electrochim. Acta*, **28**, 1 (1983).
53. J. Durst, A. Siebel, C. Simon, F. Hasché, J. Herranz, and H. A. Gasteiger, *Energy Environ. Sci.*, **7**, 2255 (2014).
54. M. Bernt, A. Hartig-Weiß, M. F. Tovini, H. A. El-Sayed, C. Schramm, J. Schröter, C. Gebauer, and H. A. Gasteiger, *Chem. Ing. Tech.*, **92**, 31 (2020).
55. M. Fathi Tovini, A. Hartig-Weiß, H. A. Gasteiger, and H. A. El-Sayed, *J. Electrochem. Soc.*, **168**, 014512 (2021).
56. C. C. L. McCrory, S. Jung, I. M. Ferrer, S. M. Chatman, J. C. Peters, and T. F. Jaramillo, *JACS*, **137**, 4347 (2015).
57. S. Geiger et al., *Nat. Catal.*, **1**, 508 (2018).
58. T. Reier, D. Teschner, T. Lunkenbein, A. Bergmann, S. Selve, R. Kraehnert, R. Schlögl, and P. Strasser, *J. Electrochem. Soc.*, **161**, F876 (2014).
59. L. D. Burke and E. J. M. O'Sullivan, *J. Electroanal. Chem. Interfacial Electrochem.*, **117**, 155 (1981).
60. E. N. El Sawy and V. I. Birss, *J. Mater. Chem.*, **19**, 8244 (2009).
61. S. Cherevko, S. Geiger, O. Kasian, A. Mingers, and K. J. J. Mayrhofer, *J. Electroanal. Chem.*, **774**, 102 (2016).
62. G. S. Harzer, J. N. Schwämmlein, A. M. Damjanović, S. Ghosh, and H. A. Gasteiger, *J. Electrochem. Soc.*, **165**, F3118 (2018).
63. S. Cherevko, S. Geiger, O. Kasian, A. Mingers, and K. J. J. Mayrhofer, *J. Electroanal. Chem.*, **773**, 69 (2016).
64. P. Jovanovič et al., *JACS*, **139**, 12837 (2017).
65. M. Lopez, A. Schleunung, and P. Biberbach, *EU Patent EP*, 1 701 790 B1 (2009), Awarded Sept. 16.
66. A. Hartig-Weiss, M. Miller, H. Beyer, A. Schmitt, A. Siebel, A. T. S. Freiberg, H. A. Gasteiger, and H. A. El-Sayed, *ACS Appl. Nano Mater.*, **3**, 2185 (2020).
67. M. Pourbaix, *Atlas of Electrochemical Equilibria in Aqueous Solutions* (National Association of Corrosion Engineers, Houston, Texas) p. 375 (1974).
68. D. Yang, B. Li, H. Zhang, and J. Ma, *Int. J. Hydrogen Energy*, **37**, 2447 (2012).
69. M. Xiao et al., *Angew. Chem. Int. Ed.*, **58**, 9640 (2019).
70. E. Antolini, *ACS Catal.*, **4**, 1426 (2014).
71. P. Piela, C. Eickes, E. Brosha, F. Garzon, and P. Zelenay, *J. Electrochem. Soc.*, **151**, A2053 (2004).
72. L. Gancs, B. N. Hult, N. Hakim, and S. Mukerjee, *Electrochem. Solid-State Lett.*, **10**, B150 (2007).
73. E. Antolini, *J. Solid State Electrochem.*, **15**, 455 (2011).
74. T. T. H. Cheng, N. Jia, and P. He, *J. Electrochem. Soc.*, **157**, B714 (2010).
75. W. Gu, P. T. Yu, R. N. Carter, R. Makharia, and H. A. Gasteiger, *Local H2 Starvation in Modern Aspects of Electrochemistry*, **49**, 45 (2010).
76. T. Reier, M. Oezaslan, and P. Strasser, *ACS Catal.*, **2**, 1765 (2012).
77. C. Fan, C. Chen, J. Wang, X. Fu, Z. Ren, G. Qian, and Z. Wang, *Sci. Rep.*, **5**, 11712 (2015).